UNIVERSITÀ DEGLI STUDI DI TORINO

FACOLTÀ SI SCIENZE MATEMATICHE, FISICHE E NATURALI

CORSO DI LAUREA MAGISTRALE IN FISICA DELLE INTERAZIONI FONDAMENTALI

Tesi di Laurea

Study of the Υ Polarization in the ALICE Dimuon Spectrometer

Relatore:
Prof. Ermanno Vercellin

Candidato:
Livio Bianchi

Co-Relatore:
Dott.sa Roberta Arnaldi

Controrelatore:
Prof. Ernesto Migliore

ANNO ACCADEMICO 2007-2008

A chi ha creduto in me

Ringraziamenti

Eccomi qui. Dopo dieci mesi di tesi e quindici giorni di intenso uso di penna e calamaio. Eccomi a ritagliarmi il tempo per dare ciò che devo a chi lo merita.

Ringrazio innanzi tutto il mio relatore prof. Ermanno Vercellin, punto di riferimento in tutto il mio percorso di tesi e sempre disponibile a prestare orecchio ai miei progetti. Un grazie molto particolare al mio co-relatore Roberta Arnaldi e a Enrico Scomparin, che per tutto questo tempo mi hanno accompagnato con i loro consigli e che non hanno mai esitato a dare spazio a qualsiasi mia domanda, anche la più stupida; l'assiduità e la simpatia con cui mi hanno seguito sono state per me estremamente preziose.
Voglio inoltre ringraziare gli altri appartenenti al gruppo di lavoro, che con la loro cordialità mi hanno fatto sentire parte di qualcosa: grazie quindi al prof. Chiavassa e al prof. Gallio, ad Alfredo, Anna, Nora, Chiara, Pietro, Roberto, Alessandro, Martino, Diego (che peraltro mi è stato più volte d'aiuto nell'atavica lotta tra l'uomo e la macchina...anche se ho l'impressione che abbia poi vinto la macchina!).

Questo lavoro non rappresenta soltanto la sintesi di 10 mesi di tesi, ma anche la chiusura dei miei anni da studente universitario, anni durante i quali la presenza di alcune persone ha reso meno pesante la frequenza delle lezioni (anche se non è mai stata troppo assidua...!).
Tra tutte queste persone voglio ringraziare in particolare Chiara e Dario, i miei primi compagni di banco con i quali ho dato nomignoli un po' a tutti, e insieme a loro Edo, Grazia e Marco: tutta gente che ho conosciuto quando non era com'è adesso, e che ho visto plagiare dal sacro fuoco della Fisica (chi più chi meno). Grazie ad Ale Jakob perché oltre ad aver detto "un sacco di stupidate" con me, l'ho sempre guardato con una certa ammirazione. Con lui ringrazio Dani, Ema, Cri, Davide, Marco, Francesco

per la gita invernale a Ginevra, e qualcuno di loro lo ringrazio anche per le scorribande notturne delle quali se non ci fossero le foto a testimoniare la vicenda non avrei certamente fatto parola! Ringrazio Luca e Walter perché con loro ho condiviso la fatica del ritardatario. Ringrazio Fede per avermi accolto quando clandestino mi aggiravo con Moli e Ale (che ringrazio) per i vicoli del CERN in cerca di qualcosa da curiosare. Grazie ad Ale, che si merita una menzione (no Ale...non quella!) particolare; lo ringrazio per l'amicizia e per i panini pane e lardo, e anche per le lunghe e inconcludenti chiacchierate su cose che né conoscevamo né ci sforzavamo di conoscere: tempo perso, ma che ricorderò con piacere.

Grazie agli amici non fisici, che di fisica proprio non vogliono sentir parlare. Grazie Gabry e Diego (hey boys!), grazie alla compagnia della mitica vacanza a Riccione tra bomboloni e baia. Grazie a Giulia, per le feste in rosso e le risikate a casa sua, e per tutto il resto. Grazie a Claudio, per le lunghe serate birra e parole e per non aver guardato il rigore di Grosso nella finale dei mondiali, e per tutto il resto.

Grazie ai miei nonni tutti: la loro testimonianza, a tratti semplice a tratti straordinaria, ha molto pesato sul mio modo di concepire e percepire la vita...e per questo li ringrazio.
Grazie a Vivi, che dal secondo anno di università ha costantemente riempito le mie giornate in modo frizzante: grazie per aver tinto con colori pastello la mia quotidianità.
E infine il primo Grazie: ai miei genitori, che mi hanno prima cullato, poi guidato e infine seguito, e senza i quali sarebbe stato difficile pensare in grande.

Ah...dimenticavo...a te che stai leggendo queste due pagine: se non hai trovato il tuo nome sappi che ringrazio anche te.

Contents

Introduction

As far as we know Nature behaves according to two physics theories named Standard Model and General Relativity: the first one describes electro-weak and strong interactions while the second one gravitation. The connections between these two theories are not evident and the unification of the two is one of the most important challenges of physics research for the future.

Standard Model is a Yang-Mills field theory based on the gauge group $SU(3) \times SU(2) \times U(1)$, with QCD (Quantum Cromo-Dynamics - the SU(3) part) describing the strong interactions.

Even if QCD seems to describe in a satisfactory way the strong interaction, we are not yet able to extract from it in a controlled way a great part of hadron properties. Furthermore, the study of phase transitions involving strongly interacting particles is a rapidly evolving field of QCD. In particular, the study of the transition from a confined hadronic system towards a plasma of quarks and gluons (QGP) has received a lot of attention, both theoretically and experimentally, in the past 20 years.

Quarkonium systems may be crucially important to improve our understanding of QCD. They probe all the energy regimes of QCD, from the hard region, where an expansion in the coupling constant is possible, to the low-energy region, where nonperturbative effects dominate. Heavy quark-antiquark bound states are thus an ideal, and to some extent, unique laboratory where our understanding of nonperturbative QCD may be tested in a controlled framework. Moreover, the yield of heavy quarkonium states is predicted to be suppressed in a system which has reached deconfinement.

The study of heavy quarkonium production has been theoretically investigated for many years and nowadays the most successful approach is represented by the so-called NRQCD model, which has been able to satisfactorily explain the heavy

quarkonia cross sections measured by CDF.
Apart from cross sections, NRQCD can also predict the behaviour of other observables and one of these observables is polarization, which has been theoretically studied both for hadronic collisions and for ion collisions. The polarization of an unstable particle is analyzed by the angular distribution of the decay products.

ALICE is the dedicated heavy-ion experiment at the LHC. By colliding Pb ions at $\sqrt{s} = 5.5$ TeV/nucleon it will be possible to create and study a hot, extended and deconfined system of partons. Furthermore, the study of p-p collisions will allow to obtain reference data for QGP studies, but also to investigate in detail many aspects of QCD.

Thanks to its muon and electron detection capabilities, ALICE can measure quarkonium production over a large rapidity range in both p-p and Pb-Pb collisions. In the following an investigation of the physics capabilities for the measurement of the Υ polarization in the Forward Muon Spectrometer of ALICE has been carried out.

In the first Chapter an introduction to quarkonium and to its main features can be found, mainly focusing on what quarkonia can probe both in p-p and Pb-Pb collisions. Polarization study is discussed in Chapter 2, where an overview of the experimental data obtained until now is presented and briefly discussed; in the same chapter a discussion on experimental tools for the polarization analysis can also be found. Chapter 3 is about the ALICE experiment: the central barrel is sketched out, while the muon spectrometer is analyzed in more detail; a short description of the ALICE software framework is also carried out. The description of the polarization analysis on simulated data for both p-p and Pb-Pb collisions can be found in Chapter 4, while in Chapter 5 conclusions and future perspectives are presented.

Chapter 1

Heavy Quarkonia

The term "Heavy Quarkonia" refers to unflavored mesons composed by c or b quarks. Given their high mass, the motion of c and b quarks within the bound state is to a good extent non-relativistic and non-perturbative. Heavy quarkonia production is usually considered as a two-stage process: a perturbative $q\bar{q}$ production mechanism is followed by a non-perturbative stage where the bound state is formed. In *Section 1.1* a brief presentation of the $c\bar{c}$ and $b\bar{b}$ states is carried out as well as a list of the main properties; the problem of the production mechanism is analyzed in *Section 1.2* while in *Section 1.3* quarkonium as a probe of the medium is considered.

1.1 Spectroscopy

The lower-mass states of heavy quarkonium resonances are rather stable particles: due to their mass below the threshold for open heavy flavored meson pair production, their decay modes are either electromagnetic or OZI-suppressed (about 30% and 70% respectively, for charmonium). The ground state for $c\bar{c}$ vector mesons is the J/ψ ($m_{J/\psi} \simeq 3,1GeV$, $\Gamma = 91keV$), while the ground state for $b\bar{b}$ vector mesons is the Υ ($m_{\Upsilon} \simeq 9,5GeV$, $\Gamma = 53keV$). The excited states below the open charm/beauty threshold have widths ranging from a few dozens keV to a few dozens MeV. A list of the heavy quarkonium states is shown in *Figure 1.1*.

The spectroscopy of quarkonia is phenomenologically described by assuming that the $q\bar{q}$ pair is subjected to the Cornell potential, consisting of a Coulomb-like term accounting for gluon-exchange between the two quarks, and a confining term

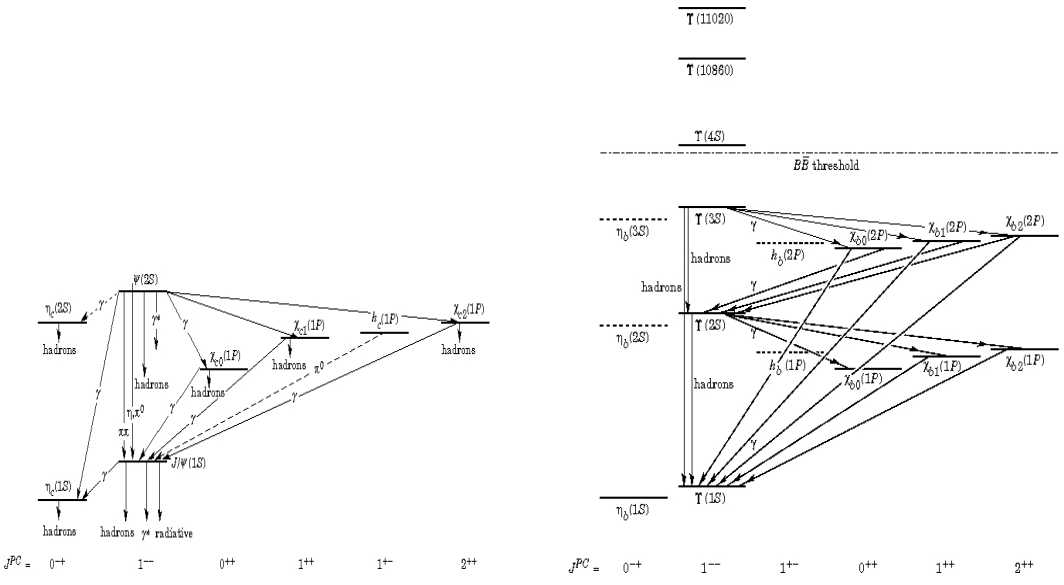

Figure 1.1: $c\bar{c}$ and $b\bar{b}$ states

parametrising the non-perturbative effects:

$$V(r) = -\frac{\alpha}{r} + kr \tag{1.1}$$

The results obtained by solving the Schrödinger equation with the potential 1.1 (and ad-hoc values of the parameters) are in fair agreement with the observed spectra.

1.2 Production

The issue of quarkonium production mechanism is still an open research field. For what concerns the identification of the partons involved in the production of the $q\overline{q}$ pairs, earlier experiments ruled out the hypotesis of electromagnetic production via $q\overline{q}$ annihilation, since it was shown that the production rate of J/ψ is identical in $\pi^+ - N$ and $\pi^- - N$ collisions (the difference in electric charge between the u and d quarks should suppress the production in $\pi^+ - N$ collisions by a factor 4). Similarly, the hypotesis of $q\overline{q}$ annihilation into a gluon as the main production process was rejected after the comparison between the production rate in $p-\overline{p}$ and in $p-p$ collisions, since the difference between the $\overline{q}$ content of proton and antiproton

should lead to a suppression in $p-p$ by a factor $5 \div 10$, which is not observed. Thus quarkonium production proceeds mainly via gluon fusion ($gg \rightarrow q\overline{q}$) or gluon fragmentation.

In both heavy-quarkonium annihilation decays (no heavy quark in the bound state) and hard-scattering production, large energy-momentum scales appear. The heavy-quark mass m is much larger than Λ_{QCD} and, in the case of production, the transverse momentum p_T can be much larger than Λ_{QCD} as well. This implies that the associated values of the QCD running coupling constant are much smaller than 1 ($\alpha_S(m_c) \approx 0.25$ and $\alpha_S(m_b) \approx 0.18$). Therefore, one might hope that it would be possible to calculate the rates for heavy quarkonium decay and production accurately in perturbation theory.
However, there are low-momentum, non-perturbative effects associated with the dynamics of the quarkonium bound state that invalidate the direct application of perturbation theory.

In order to make use of perturbative methods, one must first separate the short-distance/high-momentum perturbative effects from the long-distance/low-momentum nonperturbative effects; such a process is known with the name of *factorization* and nowadays is the basic approach to the problem of quarkonium production.

Some models were developped in the years to describe theoretically or phenomenologically the quarkonia production mechanism and such models have been tested in the 90s on data collected at Tevatron. In the following a brief description of these models is carried out.

1.2.1 Color Evaporation Model (CEM)

The Color Evaporation Model is the most phenomenological one and was first proposed in 1977 [22, 23, 27, 34]. In the CEM, the production cross-section for a quarkonium state H is a certain fraction F_H of the cross-section for producing $q\overline{q}$ pairs with invariant mass below the $M\overline{M}$ threshold, where M is the lowest mass meson containing the heavy quark q. This cross-section has therefore an upper limit on the $q\overline{q}$ pair mass but no constraints on the color or spin of the final state. The $q\overline{q}$ pair is assumed to neutralize its color by interaction with the collision-induced color field by "color evaporation". If the $q\overline{q}$ invariant mass is less than the heavy-meson threshold $2m_M$, then the additional energy that is needed to produce heavy-flavoured hadrons

can be obtained from the nonperturbative color field. Thus, the sum of the fractions F_H over all quarkonium states H can be less than unity.
The fractions F_H are assumed to be universal so that, once they are determined by data, they can be used to predict the cross-sections for other processes and for other kinematic regions.

In the CEM at leading order in α_s, the production cross-section for the quarkonium state H in collisions of the light hadrons h_A and h_B is:

$$\sigma_{CEM}^{(LO)}[h_A h_B \to H + X] = \\ = F_H \sum_{i,j} \int_{4m_q^2}^{4m_M^2} d\hat{s} \int dx_1 dx_2 f_i^{h_A}(x_1,\mu) f_j^{h_B}(x_2,\mu) \hat{\sigma}_{ij}(\hat{s}) \delta(\hat{s} - x_1 x_2 s) \quad (1.2)$$

where:

- h_A and h_B are the colliding hadrons;
- ij corresponds to $q\overline{q}$ and gg pairs;
- $\hat{\sigma}_{ij}$ is the $ij \to q\overline{q}$ sub-process cross-section;
- $f_i^{h_A}(x_1,\mu)$ and $f_j^{h_B}(x_2,\mu)$ are the parton densities in the colliding hadrons.

The leading-order calculation cannot describe the quarkonium p_T distribution, since the p_T of the $q\overline{q}$ pair is zero at LO. At NLO in α_s the subprocesses $ij \to kq\overline{q}$ (where k is a light quark, antiquark or gluon) produce $q\overline{q}$ pairs with nonzero p_T. The most recent set of F_H values have been determined from complete NLO calculations of quarkonium production in hadronic collisions.

The most basic prediction of the CEM is that the ratio of the cross-sections for any two quarkonium states should be constant, independent of the process and the kinematic region. Some variations in these ratios have been observed: for example the ratio of the cross-sections for χ_c and J/ψ are rather different in photoproduction and hadroproduction. Such variations present a serious challenge to the status of the CEM as a quantitative model for quarkonium production, but nevertheless the model is still widely used as simulation benchmark.

In *Figure 1.2* the CEM fits to the Υ production cross-sections are shown: the continuous line is the pure CEM prediction, while the dashed line shows the correction due to the so called $k_T - smearing$ method, which takes into account multiple

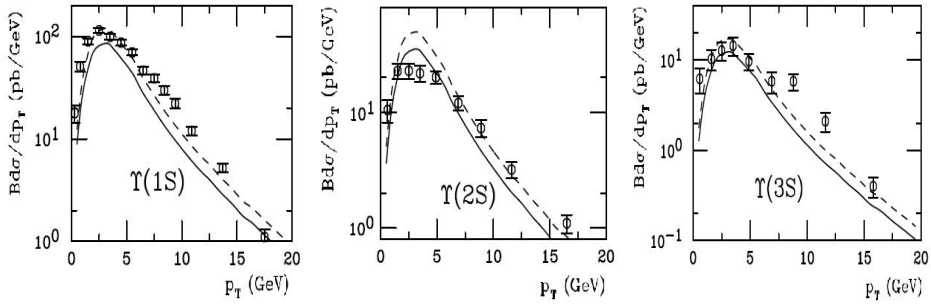

(a) (b) (c)

Figure 1.2: CEM fits to CDF data: differential cross-sections for $\Upsilon(1S)$ (1.2(a)), $\Upsilon(2S)$ (1.2(b)) and $\Upsilon(3S)$ (1.2(c)) production at Tevatron (center of mass enery of 1.8 TeV). Continuous lines show the pure CEM prediction, dashed lines show the k_T-smearing correction.

gluon emissions considering a gaussian smearing on the transverse momentum of the colliding parton.

1.2.2 Color Singlet Model (CSM)

The color-singlet model (CSM) was first proposed shortly after the discovery of the J/ψ. The main concept of the CSM is that, in order to produce a quarkonium, the $q\overline{q}$ pair must be generated with the quarkonium quantum numbers; in particular the pair has to be produced in a color-singlet state. The model can be obtained by the NRQCD formula (see later in *Section 1.2.3*) by dropping all the colour-octet terms and all but the colour-singlet term corresponding to the quantum numbers of the final resonance. Neverthless this model, though largely used in the past, is no more adopted because of two important reasons:

1. a **theoretical reason**: in case of P-wave states (or, in general, states with higher orbital angular momentum) the CSM leads to infrared divergences;

2. an **experimental reason**: data from Tevatron (CDF Run I) showed that the model underestimates the cross-sections for the production of J/ψ, $\psi(2S)$ and $\Upsilon(1S)$ by more than an order of magnitude (see *Figure 1.3*).

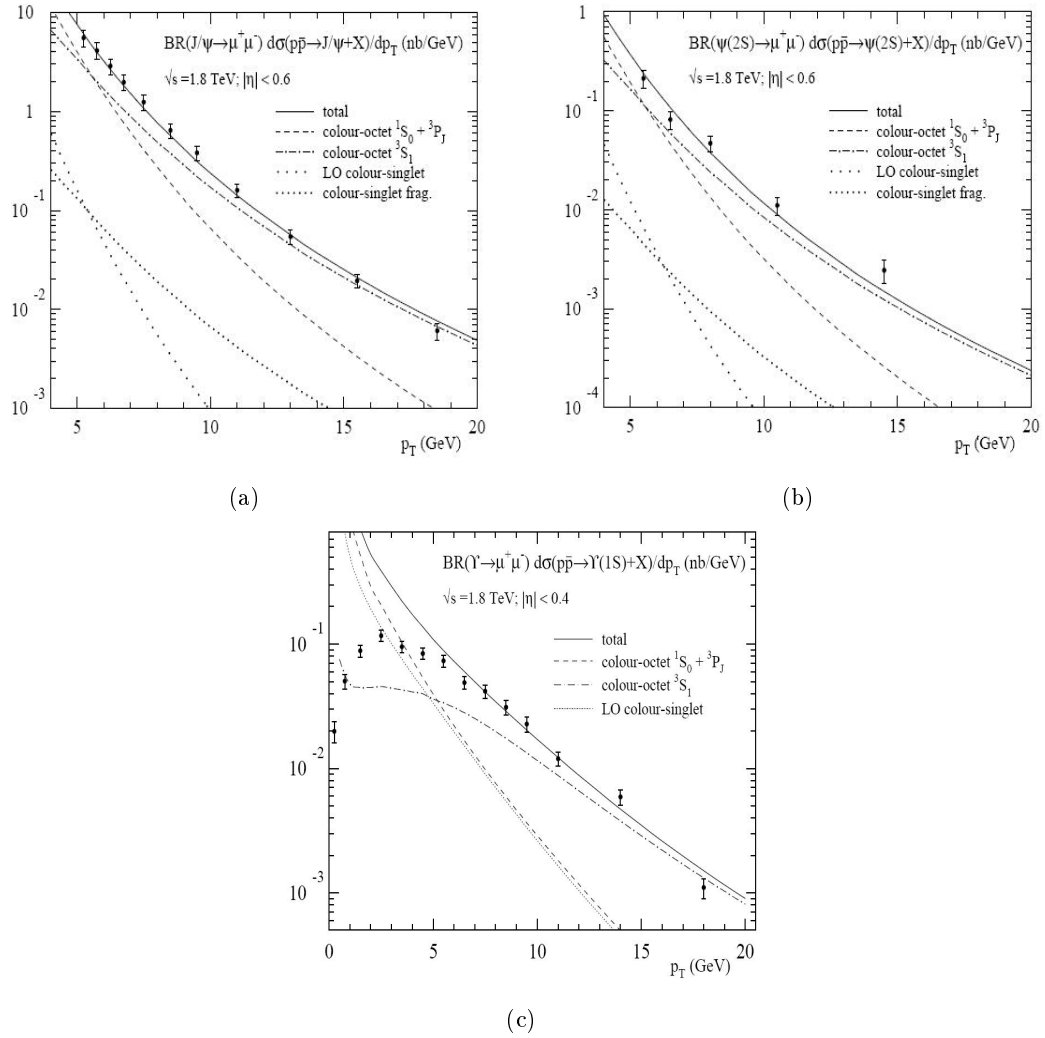

Figure 1.3: Data from CDF Run I: prompt cross-sections for J/ψ, $\psi(2S)$ and $\Upsilon(1S)$ production in $p\overline{p}$ collisions at a centre-of-mass energy of 1.8 TeV [12, 13]. Different theoretical fits are shown.

1.2.3 Non Relativistic QCD (NRQCD)

One convenient way to carry out the separation between perturbative and non-perturbative effects is through the use of the effective field theory Non Relativistic QCD (NRQCD) [7, 33, 4]. NRQCD is more than a phenomenological model since it reproduces full QCD accurately at momentum scales of order mv and smaller, where v is the typical heavy-quark velocity in the bound state in the CM frame ($v^2 \approx 0.3$ for charmonium, and $v^2 \approx 0.1$ for bottomonium). Virtual processes involving momentum scales of order m and larger can affect the lower-momentum processes, and their effects are taken into account through the short-distance coefficients of the operators that appear in the NRQCD action.
Because $q\overline{q}$ production occurs at momentum scales of order m or larger, it manifests itself in NRQCD through contact interactions. As a result, the inclusive cross-section for the direct production of the quarkonium H at large transverse momentum (p_T of order m or larger) in hadron or e-p colliders can be written as a sum of products of NRQCD matrix elements and short-distance coefficients:

$$\sigma[H] = \sum_n \sigma_n(\Lambda)\ \langle 0|\mathcal{O}_n^H|0\rangle \tag{1.3}$$

where:

- H is the quarkonium state to be produced;
- n runs over all the quantum numbers of the $q\overline{q}$ pair (color, angular momentum, spin, ...);
- Λ is the ultraviolet cutoff of the effective theory;
- $\sigma_n(\Lambda)$ are the short-distance coefficients;
- $\mathcal{O}_n^H$ are the four-fermion operators.

The short-distance coefficients $\sigma_n(\Lambda)$ are essentially the process-dependent partonic cross-sections to make a $q\overline{q}$ pair, convolved with parton distributions if there are hadrons in the initial state. The $q\overline{q}$ pair can be produced in a color-singlet state or in a color-octet state. Its spin state can be singlet or triplet, and it also can have orbital angular momentum.

The four-fermion operators create a $q\overline{q}$ pair in the NRQCD vacuum, project it onto a state that in the asymptotic future consists of a heavy quarkonium plus anything, and then annihilate the $q\overline{q}$ pair. The vacuum matrix element of such an operator is the probability for a $q\overline{q}$ pair to form a quarkonium plus anything. These matrix elements are somewhat analogous to parton fragmentation functions. They contain all of the nonperturbative physics associated with the evolution of the $q\overline{q}$ pair into a quarkonium state.
An important property of the matrix elements, which greatly increases the predictive power of NRQCD, is the fact that they are universal, i.e., process independent; they can be calculated in lattice simulations or determined from phenomenology.

NRQCD power-counting rules (for more details see [4]) allow one to organize the sum over operators in *Equation 1.3* as an expansion in powers of v. Through a given order in v, only a finite set of matrix elements contributes. The relative importance of the terms in the factorization formula is determined not only by the sizes of the matrix elements but also by the sizes of the perturbative coefficients. The size of the coefficient depends on its order in α_S, color factors and dimensionless kinematic factors such as m^2/p_T^2.

In practical calculations of the rates of quarkonium decay and production, a number of significant uncertainties arises. In many instances, the series in α_S and v in the factorization formula in *Equation 1.3* converge slowly, and the uncertainties from their truncation are large (sometimes 100% or larger). In addition, the matrix elements are often poorly determined, either from phenomenology or lattice measurements, and the important linear combinations of matrix elements vary from process to process, making tests of universality difficult. There are also large uncertainties in the heavy-quark masses (approximately 8% for m_c and approximately 2.4% for m_b) that can be very significant for quarkonium rates that are proportional to a large power of the mass.

Many of the largest uncertainties in the theoretical predictions, as well as some of the experimental uncertainties, cancel in the ratios of cross-sections, like:

$$R_\psi = \frac{\sigma[\psi(2S)]}{\sigma[J/\psi]}.$$

Another set of observables in which many of the uncertainties cancel out consists of polarization variables, which can be defined as ratios of cross-sections for the production of different spin states of the same quarkonium (see *Chapter 2*).

The NRQCD is in good agreement with data from CDF Run I for what concerns J/ψ and $\psi(2S)$ production cross-sections (see *Figure 1.3*), but seems to fail in the case of $\Upsilon(1S)$ at low-p_T because the NRQCD curve diverges like $1/p_T$ when $p_T \to 0$. In reality the problem is also present for charmonium and it could have been seen in the plot if the cross sections for J/ψ and $\psi(2S)$ were measured at lower values of p_T.
This unphysical behaviour of the NRQCD curves is an artifact of fixed-order perturbation theory and could be removed by carrying out the appropriate resummation of soft gluons (for more details see [14] pages 460 and beyond).
In conclusion NRQCD has been chosen to be in fine agreement with experimental results on quarkonium production cross-sections. The measurement of polarization, as will be detailed in *Chapter 2*, represents a further important test for the model.

1.3 Quarkonia as a probe of the medium

As described so far, quarkonia are an important probe in hadron collisions because they allow to explore the whole QCD energy-range. Moreover they play an important role in the determination of the QCD phase diagram because they can be considered as one of the most important probes for the phase transition from hadrons to a plasma of deconfined quarks and gluons (QGP). In this section an explanation of what is QGP and of the importance of quarkonium states for this study is carried out.

1.3.1 Quark-Gluon Plasma

One of the most important features of strong interactions is confinement. In a potential description it can be formulated with an effective binding-potential which increases linearly with the quark distance:

$$V_0(r) \sim \sigma r,$$

where the string tensor σ accounts for the energy per unit separation distance. Hadrons are color singlet states of colored quarks; therefore ordinary nuclear matter is a color insulator.

In a medium of electric charges a transition from electric insulator to conductor occurs when the electric charge density is increased over a critical value. This is due to the so-called Debye screening of the interaction length. The Debye screening radius r_D depends on the medium charge density; once it becomes less than the atom binding radius, the electrons can move freely and the medium becomes a plasma of unbound electric charges.

In analogy to this transition, QCD predicts that for high nuclear densities color charge is screened and quarks are no longer confined into hadrons. The medium is then transformed from an insulator to a color conductor and hadronic matter turns into a plasma of deconfined quarks and gluons; this is the so-called Quark-Gluon-Plasma (QGP).

Therefore at sufficiently high color charge density the interaction potential between two quarks includes a screening term, becoming:

$$V(r) \sim \sigma r \left[\frac{1 - e^{-\mu r}}{\mu r} \right]$$

where the screening mass μ corresponds to the inverse of the Debye screening radius r_D; hadrons whose dimensions are of the order of the μ parameter are melted.

The theoretical basis for the QGP search is given by lattice-QCD calculations that predict a critical energy density value ϵ_c for the transition of the order of $\sim 1\ GeV/fm^3$. High energy densities can be obtained either by increasing temperature or the net baryon density. The critical deconfinement temperature T_c at baryon chemical potential $\mu_B = 0$ is about 170 MeV. Ultra-relativistic heavy-ion collisions allow the investigation of the QCD phase-diagram (see *Figure 1.4*).

1.3.2 Quarkonia suppression as a probe of deconfinement

The suppression of heavy quarkonia in a deconfined medium was first discussed in 1986 [29]. The prediction is based on the screening effect of deconfined color charges on the $q\overline{q}$ binding: since the formation of quarkonium resonances happens on timescales compatible with the formation of the plasma, they are a probe of the hot and dense matter created in the collision and may be influenced by its properties.

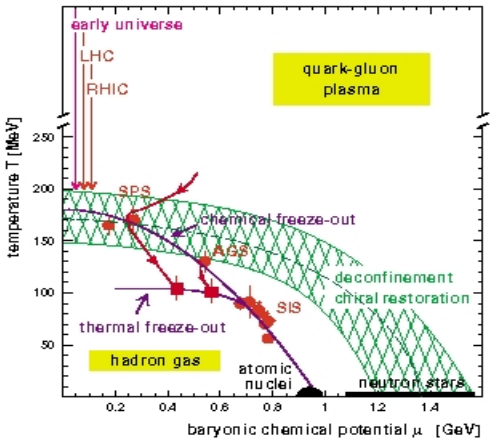

Figure 1.4: QCD phase-diagram: transition to the deconfined state (QGP)

When the temperature reaches the critical value T_C, deconfinement sets in and the confining term in the Cornell potential *1.1* disappears. Moreover, the Coulomb-term must be modified to take into account color screening of the potential, which becomes:

$$V(r) = -\frac{\alpha}{r} e^{-\frac{r}{r_D}} \tag{1.4}$$

The screening radius r_D decreases with increasing temperature: its estimation is mainly based on Lattice QCD calculations, which indicate a behaviour proportional to $T^{-1/2}$. When minimising the energy of the bound state as a function of the resonance radius, using the potential *1.4*, one finds a minimum value of r_D for which there is a solution, i.e. there is a value of r_D below which the resonance can not form, thus a temperature above which the resonance is suppressed (see *Figure 1.5*). Subsequently the two heavy quarks travel in the medium without binding until hadronization, when they finally form open charm or open beauty mesons.

Since different quarkonium resonances have different binding energies, and thus different dimensions, it is expected that those states who are less tightly bound should melt at lower temperatures: the sequential suppression of resonances may be interpreted as a "thermometer" for the plasma [30].

While the argument of quarkonia suppression in a deconfined medium lies on solid theoretical bases, nevertheless the validation of predictions against the experiment is not straightforward, since there are a set of concurrent or alternative processes

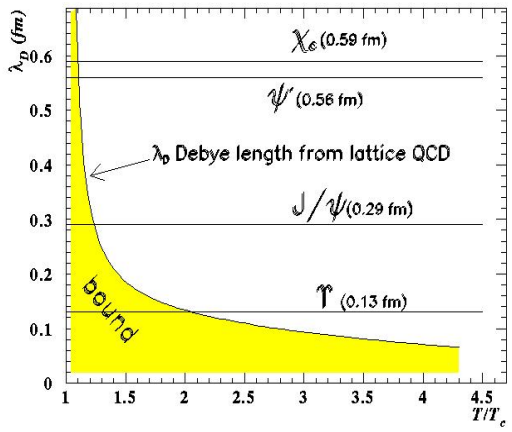

Figure 1.5: Debye screening redius in a deconfined medium, as a function of T/T_C, compared with estimates for the radius of a few quarkonium resonances.

which may blur the picture. These include:

- cold nuclear matter effects affecting the quarkonia yield in both the initial state (e.g. shadowing of the Parton Distribution Functions in the nucleus) and the final state (nuclear absorption); these are somewhat known effects that can be taken into account in the analysis of data;

- quarkonia suppression in a hadronic medium, by the so-called "hadronic co-movers";

- quarkonia regeneration phenomena.

1.3.3 Experimental results on quarkonia suppression

In this section a few experimental issues related with the sudy of J/ψ suppression will be discussed, and some results on J/ψ suppression will be summarized. Results on bottomonium states so far are scarce, due to a smaller production cross section.

J/ψ was preferably studied through its dileptonic decays: the measured branching ratio is similar for e^+e^- and $\mu^+\mu^-$ (about 6%).

The J/ψ suppression pattern

Information about suppression mechanisms can be obtained by measurig the J/ψ yield per nucleon-nucleon collision (N-N) as a function of the centrality of the collision. In absence of suppression mechanisms, the production yield should be proportional to the number of N-N collisions, and therefore the yield per N-N collision should be independent of centrality. The number of N-N collisions for a given centrality can be obtained from the Glauber model (for a review on the model see [32]).

A few experiments have chosen to study (as a function of centrality) the ratio of the J/ψ yield to the Drell-Yan yield. The latter process has a production cross-section proportional to the number of N-N collisions, but it is not affected by the medium. Its measurement is subjected to similar experimental systematics (acceptance, trigger and so on) as those affecting the measurement of J/ψ dileptonic decays: such systematics cancel when computing the ratio.

As pointed out in *Section 1.3.2*, cold nuclear matter effects affect the J/ψ yield, causing what is called the "normal" suppression. Such phenomena include the absorption by nucleons in the colliding nuclei: this effect, also referred to as nuclear absorption, can be parametrized with a phenomenological absorption cross-section σ_{abs}, so that:

$$\sigma(AB \to J/\psi) \propto ABe^{-\rho_0 \sigma_{abs} L}$$

where A and B are the numbers of nucleons in the two colliding nuclei, ρ_0 is the ordinary nuclear density and L is the length of the path of the $c\bar{c}$ pair through nuclear matter, which can be calculated from the impact parameter of the collision. These centrality variables are computed in the frame of the Glauber model. The value of σ_{abs} is usually obtained experimentally from p-A or d-A collisions, where only normal J/ψ suppression is possible.

Overview of experimental results

The main results on quarkonia suppression come from NA38, NA50 and NA60 (see *Figure 1.6*) experiments at SPS and from the PHENIX experiment at RHIC.

The NA38 experiment measured J/ψ production in O-U and S-U collisions (200 GeV/nucleon) by means of a dedicated muon spectrometer: a factor 2 suppression of the J/ψ yield from peripheral to central collisions was observed [17]. It was shown

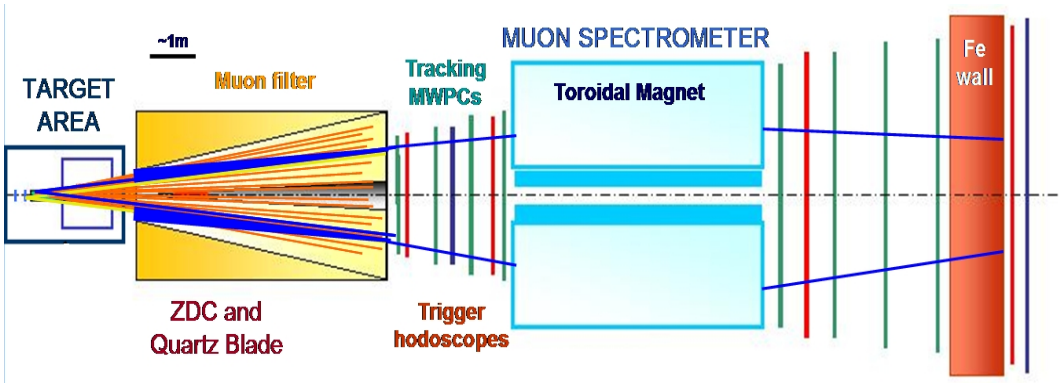

Figure 1.6: Design of the NA50 experiment: the vertex tracker in the target area was only added with the upgrade to NA60.

that such suppression was compatible with nuclear absorption [15].

The NA50 experiment (an upgrade of the previous NA38) took data in heavier ion collisions, such as Pb-Pb at 158 GeV/nucleon, where the energy density created is larger: a strong deviation from the normal suppression pattern was indeed observed [16]. The suppression pattern obtained by NA50 is shown in *Figure 1.7*, together with the NA38 data and their extrapolation according to the nuclear absorption pattern.

The NA50 experiment was later upgraded to NA60 by adding a vertex tracker, drastically improving the mass resolution and the rejection of background. The results obtained by NA60 [21] in In-In collisions confirm the suppression observed by NA50, with an onset of the suppression at an energy density around 1.5 GeV/fm^3. Models predicting J/ψ suppression by comovers in an expanding hadronic gas fail to account for the entity of the observed suppression [28]. All these experiments also carried out measurements of J/ψ production in p-A collisions, which were essential to determine the size of normal nuclear absorption.

The start-up of RHIC opened the way to a new energy domain for heavy ion collisions, with an increase in $\sqrt{s}$ of about one order of magnitude (from 17 to 200 GeV per nucleon pair). The J/ψ suppression pattern at RHIC has been mainly

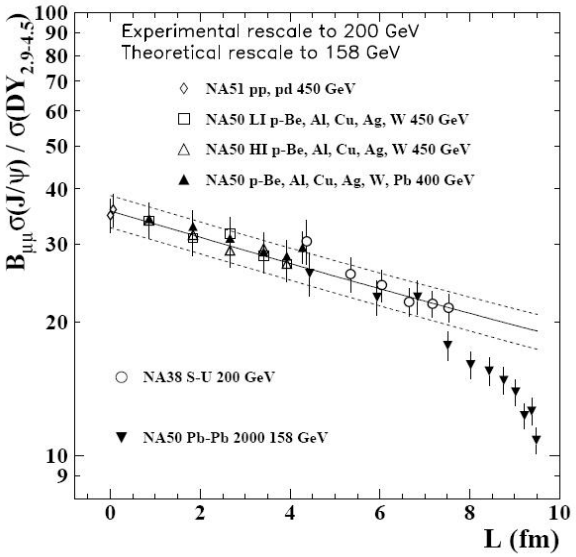

Figure 1.7: Ratio of J/ψ to Drell-Yan cross-section as a function of the path length L, as measured by NA38 and NA50. The fit of p-A data according to the nuclear absorption hypotesys is also shown.

investigated by the PHENIX experiment (see *Figure 1.8* for the apparatus). J/ψ is detected in both the dimuon (at forward rapidity) and dielectron (at midrapidity) decay channel.

The chioce of normalizing the J/ψ yield to another reference process (such as Drell-Yan) is useful, but not mandatory: in fact the PHENIX collaboration chose to compare the A-A data directly to p-p, by studying the *nuclear modification factor*:

$$R_{J/\psi}^{AA} = \frac{d^2N_{J/\psi}^{AA}/dp_T dy}{N_{coll} d^2N_{J/\psi}^{pp}/dp_T dy} \tag{1.5}$$

where N_{coll} is the number of collisions, $d^2N_{J/\psi}^{AA}/dp_T dy$ the number of J/ψ for a given p_T and a given y for ion-ion collisions and $d^2N_{J/\psi}^{pp}/dp_T dy$ the same quantity for proton-proton collisions. $R_{J/\psi}^{AA}$ (when integrated over p_T and y) is basically the ratio between the J/ψ yield per nucleon collision in A-A and the same quantity in p-p and it depends on the centrality of the collision.

The results obtained by PHENIX on J/ψ suppression in Au-Au and Cu-Cu collisions [26] have been puzzling the heavy ion community, since it looks like the amount

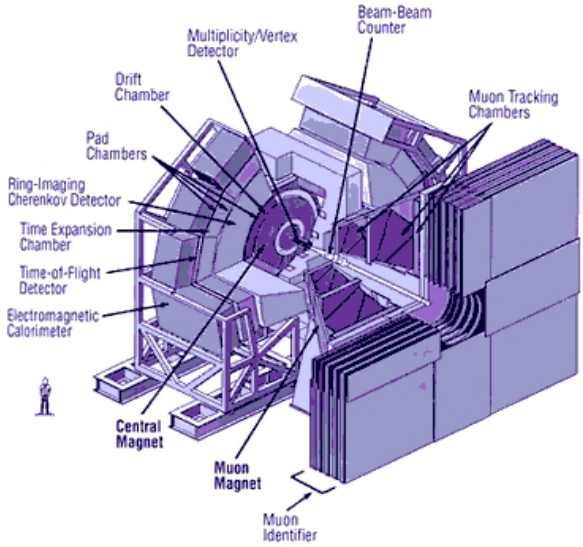

Figure 1.8: Right-half of the PHENIX experimental apparatus.

of suppression observed at RHIC is pretty much the same as the one observed at SPS, as can be seen in *Figure 1.9*.

Two differnt hypoteses have been made to explain this feature of the results.

- **Sequential suppression -** The measured prompt J/ψ yield is composed of 60% directly produced $J/\psi(1S)$ and of 40% J/ψ produced in the decays of higher resonances such as $\psi'(2S)$ (about 10%) and $\chi_c(1P)$ (about 30%). As it was pointed out in *Section 1.3.2*, the dissociation temperature for $J/\psi(1S)$ is expected to be higher than the one for $\psi'(2S)$ and $\chi_c(1P)$: if the temperatures reached at SPS and at RHIC, though different, are both in the region between the χ_c dissociation temperature and the J/ψ dissociation temperature, then one can expect the observed suppression to be the same, since in both cases the suppression only affects the feed down and not the direct J/ψ.

- **Regeneration -** The production of charm in the thermalized medium is expected to be suppressed by the high mass of the c quark. If, anyway, a significant number of charm quarks-antiquarks is produced during the primary collision, in the hadronization stage uncorrelated $c\bar{c}$ pairs can recombine to form a J/ψ. The extra J/ψ yield thus created is expected to increase with

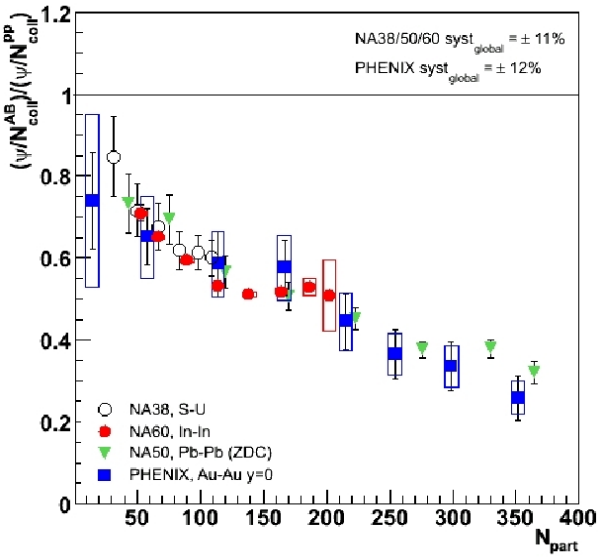

Figure 1.9: J/ψ nuclear modification factor as a function of the number of participant nucleons at RHIC and SPS.

the energy of the collision (because so does the charm cross-section): one can therefore have at RHIC a suppression of native J/ψ, partially compensated by the enhancement due to regeneration.

The two scenarios presented above lead to very different predictions for experiments at higher energies. If sequential suppression is the correct explanation, then the J/ψ should eventually melt, leading to an increased suppression; on the contrary, if regeneration is the correct explanation, then the J/ψ yield is expected to grow as more charm is produced.

The puzzle is thus expected to be solved at the Large Hadron Collider (LHC) at CERN, where Pb-Pb ions will collide at $\sqrt{s} = 5.5TeV$ per nucleon pair.

Chapter 2

Quarkonium polarization

The main subject of the dissertation is here introduced. In *Section 2.1* an explanation of what polarization is and how it can be studied from the experimental point of view is carried out. *Section 2.2* is about the predictions on the quarkonium polarization both in hadronic and in ion collision experiments, while *Section 2.3* briefly shows what are the most important experimental results on this subject.

2.1 Study of Massive Vector Mesons's Polarization

The polarization of a particle produced in a particular process measures the probability for the particle to be produced (in that specific process) with a particular spin-alignment. Spin is an intrinsic quantum number and the spin state can be specified by the total spin S and by its third componend with respect to a given z-axis S_z; considering that the way of behaving of the spin is similar to that of the angular momentum, one can depict S as a vector in the usual 3D space and S_z like its projection (quantized) along the z-axis.

Vector mesons are spin-1 states and their mass different from zero provides three possible values for the third component of the spin: +1,0,-1. A polarization measurement for a certain particle sample consists of:

- the choice of a polarization axis;
- the determination of the third component of the spin along that axis.

If $S_z = \pm 1$ we say that the particle is *transversely* polarized, while if $S_z = 0$ than the polarization is *longitudinal*[1]. If the measurement of the polarization is carried out on a large number of particles the result will be that ξ_L of them are longitudinally polarized and ξ_T are transversely polarized, where:

$$\xi_L = \frac{\sigma_L}{\sigma_{TOT}} \qquad \xi_T = 1 - \xi_L = \frac{\sigma_T}{\sigma_{TOT}} \tag{2.1}$$

From the experimental point of view, polarizations are measured using the angular distribution of daughter particles produced in a particle decay, because the spin state affects this distribution. For the case of dilepton decays the differential decay amplitude can be written as:

$$\frac{d\Gamma}{dcos\theta^*} \propto \frac{3}{2(\alpha+3)} \left(1 + \alpha\ cos^2\theta^*\right) \tag{2.2}$$

where θ^* is the polarization angle between the positive lepton direction [2] and the polarization axis in the mother particle's C.M. frame. The parameter α is the so-called "polarization parameter" and should be considered as a quantity related to polarization, but not as the polarization itself: the evidence of such a difference can be found in *Appendix A*, where the complete derivation of *Equation 2.2* is carried out. From the α parameter, ξ_L and ξ_T can be obtained:

$$\xi_L = \frac{1-\alpha}{3+\alpha} \qquad \xi_T = \frac{2(1+\alpha)}{3+\alpha} \tag{2.3}$$

The natural way to measure polarization is therefore to fit the $cos\theta^*$ distribution of the data with the *Equation 2.2*, to estimate the α parameter and then to calculate ξ_L and ξ_T.

2.1.1 Reference frame

The first choice to be done is the reference frame in which the polarization angle is extracted. Usually the mother particle's C.M. frame is chosen, but the important thing to be selected is the polarization axis, which can be defined in various ways.

[1] The reason of such a denomination has to be found in QED, where the photon properties (massless vector particle with $S_z = \pm 1$) are connected with the transversality of the electro-magnetic wave

[2] The negative lepton direction would serve equally well, but one or the other should be used consistently

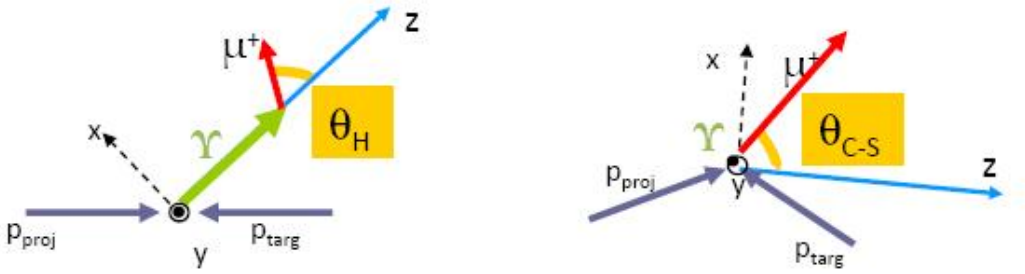

Figure 2.1: Two different reference frames where to study quarkonium polarization: Helicity (left) and Collins-Soper (right)

In collider experiments two possibilities are usually taken into account and these two lead to the definition of two different polarization angles (see *Figure 2.1*):

- Helicity angle;
- Collins-Soper angle.

The first one is the angle between the daughter particle's (positive lepton) momentum (in the quarkonium rest frame) and the direction of the mother particle's momentum in the collision C.M. frame. The second one is more related to the initial state because it is defined as the angle between the positive lepton momentum (in the quarkonium rest frame) and the bisector of the projectile momentum vector and minus the target momentum vector in the mother particle's reference frame. The helicity axis is the most used because most of the theoretical predictions have been made in this reference frame, however in fixed target experiments the Collins-Soper reference frame has been widely used.

2.2 Predictions on Quarkonia polarization

Quarkonia polarization is an important issue because the production models are able to produce specific and in some cases also accurate predictions on this subject. In this section the most important predictions are listed both for hadronic collisions and for ion collisions.

2.2.1 Hadronic collisions

As already stated in *Section 1.2.3* a set of observables in which many of the uncertainties in NRQCD cancel out consists of polarization variables because they are defined as ratios of cross-sections (see *Equation 2.1*). The NRQCD factorization approach gives the following simple prediction for the polarization variable α at very large transverse momentum.

The production of a quarkonium with p_T that is much larger than the quarkonium mass is dominated by gluon fragmentation, a process in which the quarkonium is formed in the hadronization of a gluon that is created with even larger transverse momentum. The NRQCD factorization approach predicts that the dominant gluon-fragmentation process is gluon fragmentation into a $q\overline{q}$ pair in a colour-octet ${}^3S_1$ state. The fragmentation probability for this process is of order α_s , while the fragmentation probabilities for all other processes are of order α_s^2 or higher. The NRQCD matrix element for this fragmentation process is $\langle \mathcal{O}_8^H({}^3S_1) \rangle$ (see *Chapter 1.2.3* for details).

At large p_T, the fragmenting gluon is nearly on its mass shell, and therefore is transversely polarized. Furthermore, the velocity-scaling rules predict that the colour-octet $q\overline{q}$ state retains the transverse polarization as it evolves into an S-wave quarkonium state [8], up to corrections of relative order v^2. Radiative corrections and colour-singlet production dilute the quarkonium polarization somewhat [66, 89]. In the case of J/ψ production, feed-down from higher quarkonium states is also important [78]. Feed-down from χ_c states is about 30% (10% for $\psi(2S)$) of the J/ψ sample and dilutes the polarization. Despite this effect, a substantial polarization is expected at large p_T, and its detection would be a "smoking gun" for the validity of the colour-octet production mechanism.

Considering that the CSM can be derived by the NRQCD factorization formula (1.3) retaining only the non-perturbative coefficients corresponding to a singlet $q\overline{q}$ state, the considerations on the process involved in quarkonium formation can also be applied here and so gluon fragmentation is again responsible for the production. If only singlet states are involved, the prediction is of a transverse polarization for every value of p_T.

For the CSM, since spin and color variables are not explicitely taken into account, quarkonium is produced unpolarized (the k_T-smearing approach introduces some

little corrections).

2.2.2 Ion collisions

For what concerns ion collisions, a study of how the matter affects charmonium polarization can be found in [24]; a similar study for bottomonium is not yet available. Assuming that at sufficiently high collision energies a quark-gluon plasma is formed, this will of course result in the suppression of the formation probability (see *Section 1.3.2*); moreover, the presence of the plasma is likely to affect the excited states more significantly, and the contribution of the excited quarkonium states to the observed yield of J/ψ will thus change, which also can result in a change of the J/ψ polarization. Considering these effects, the predicted α for the J/ψ in case of QGP formation is

$$\alpha_{J/\psi}^{QGP} \simeq 0.35 \div 0.4$$

for $p_T \to 0$: it is therefore expected an increase of polarization for low-p_T regions in the case of QGP formation.

2.3 Experimental results on polarization

The study of quarkonium polarization in hadron and ion collisions has been carried out by many experiments. In this section a brief overview on results from E866, NA60, HERA-B, PHENIX, CDF and D0 experiments is made.

2.3.1 E866

The first experiment considered is E866 at Fermilab Tevatron, a fixed-target experiment (shown in *Figure 2.2*) where polarization has been studied for both charmonium and bottomonium states.

For what concerns charmonium, approximately 9 million reconstructed J/ψ produced in 800 GeV ($\sqrt{s} = 38.8GeV$) proton interactions with a copper target have been analyzed in the Collins-Soper reference frame. Results are shown in *Figure 2.3(a)* and display a polarization parameter consistent with zero, with a smooth decreasing at high x_F. No strong dependence on the p_T bin seems to be present.

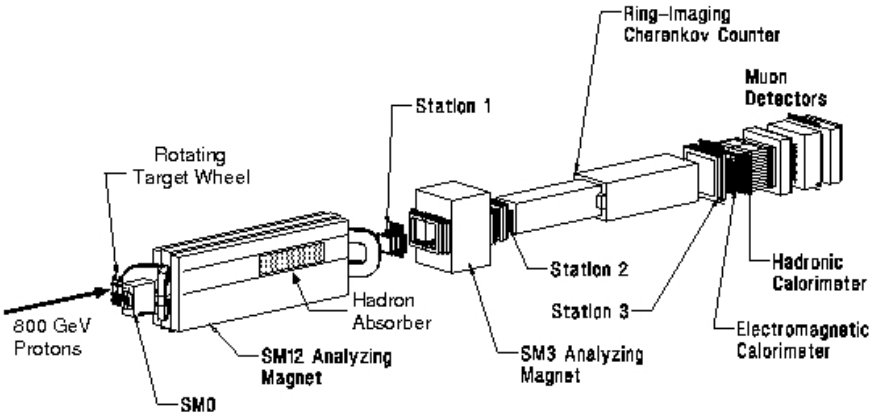

Figure 2.2: The E866 detector at Tevatron

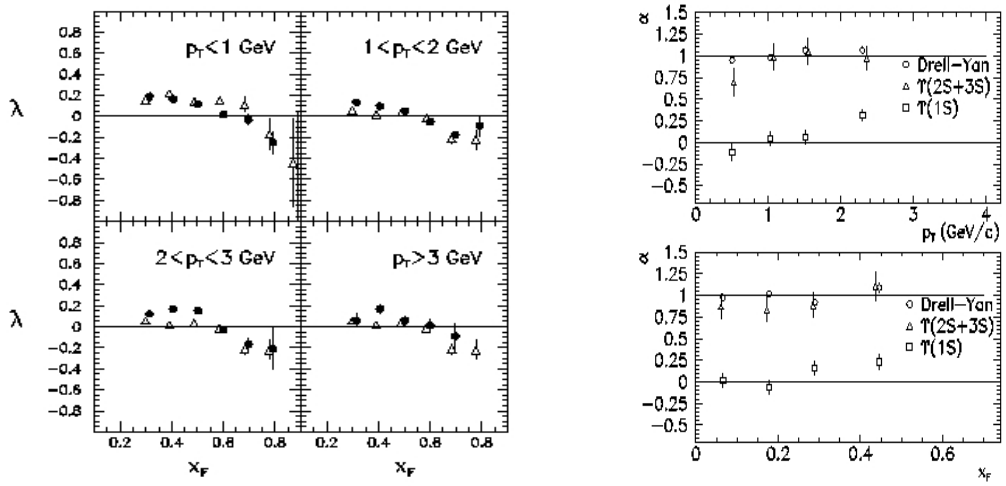

(a) (b)

Figure 2.3: The E866 measurements for the quarkonium polarization. (2.3(a)): J/ψ polarization parameter (here named λ instead of α) as a function of x_F in four p_T bins; solid dots are the results obtained with a 2800 A current in the magnet, while open triangles correspond to a 2040 A run. (2.3(b)): Υ polarization parameter as a function of p_T (up) and x_F (down).

For what concerns bottomonium, a 2 million sample of $\Upsilon(1S)$, $(2S)$, $(3S)$ and Drell-Yan produced in p-Cu collisions at 800 GeV ($\sqrt{s} = 38.8GeV$) has been analyzed in order to extract the dependence of the α parameter on p_T and x_F. The reference frame used for the analysis is again the Collins-Soper one. Results are shown in *Figure 2.3(b)* and show that for Drell-Yan and $\Upsilon(2S+3S)$ the polarization is widely transverse, while for $\Upsilon(1S)$ α is approximately equal to zero in all the ranges of p_T and x_F.

2.3.2 HERA-B

HERA-B is a fixed target experiment working on the 920 GeV proton beam of the HERA accelerator at the DESY laboratory in Hamburg. A picture overview of the detector can be found in *Figure 2.4*. During the last data taking period (2002-2003),

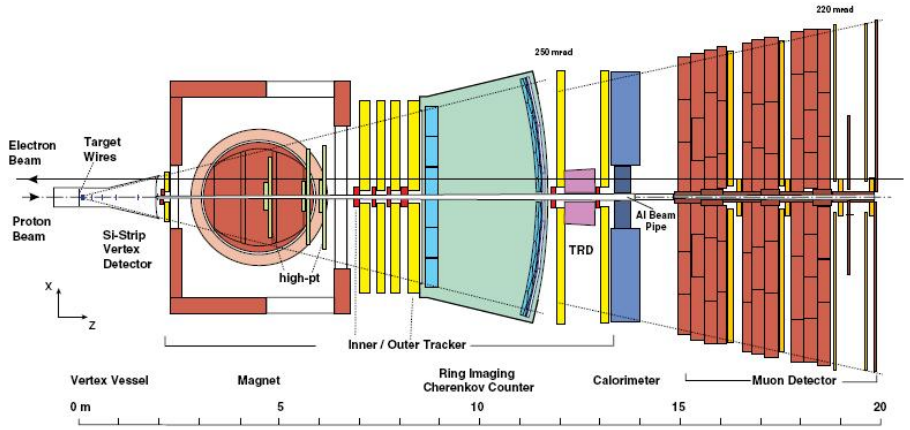

Figure 2.4: The HERA-B detector.

about 150 million dilepton triggers were acquired. These large statistics allowed detailed studies on the production of charmonium states in proton-nucleus collisions. Some preliminaries on the J/ψ polarization have been recently shown [20]. In *Figure 2.5(a)* the α parameter estimate for different p_T values is shown for three different reference frames: Helicity, Collins-Soper and Gottfried-Jackson [3]. Results show that polarization is longitudinal in the lower-p_T region and it reaches (and maintain) zero

[3] In the Gottfried-Jackson reference frame the polarization axis is chosen as the direction of the beam in the quarkonium reference frame (fixed-target experiments)

while p_T enhances. In *Figure 2.5(b)* a study of the dependence of the α parameter with respect to the target material show no significant effect.

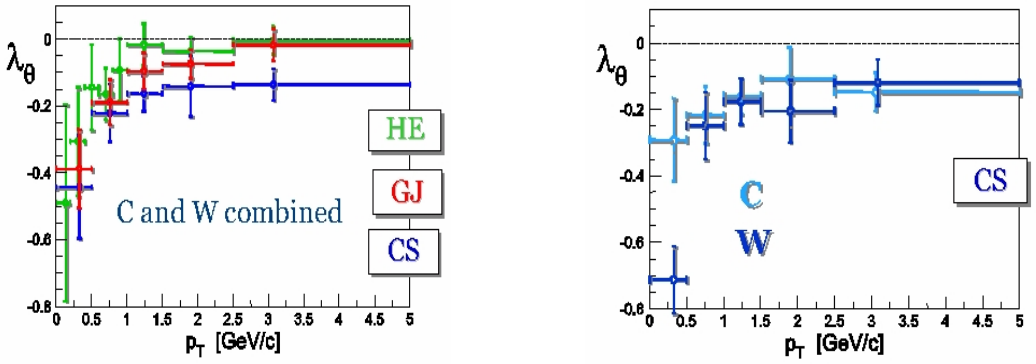

(a) (b)

Figure 2.5: HERA-B preliminary results on J/ψ polarization in p-A collisions; λ_θ corresponds to the α parameter. (a): different polarization angles. (b): different targets (C and W) in the Collins-Soper polarization angle.

2.3.3 PHENIX

The PHENIX experiment has been briefly described in *Section 1.3.3*. Thanks to its muon and electron detectors, the study of the quarkonium polarization can be carried out. Preliminary results on polarization were recently shown [3] for p-p collisions at $\sqrt{s} = 200$ GeV: this results show that for $p_T < 6$ GeV the α parameter for the J/ψ is consistent with zero (see *Figure 2.6*).

2.3.4 CDF

CDF is a collider experiment at the Tevatron accelerator (Fermilab) which studies $p - \overline{p}$ collisions. A scheme of the detector can be found in *Figure 2.7*.

Results on the polarization study from this experiment are very interesting because they can be directly compared with some theoretical predictions based on NRQCD (see [6, 5]) and on CEM.

Analysis on charmonium has been done on data recorded between June 2004 and February 2006 (Run II of the Tevatron - $\sqrt{s} = 1.96TeV$) corresponding to an inte-

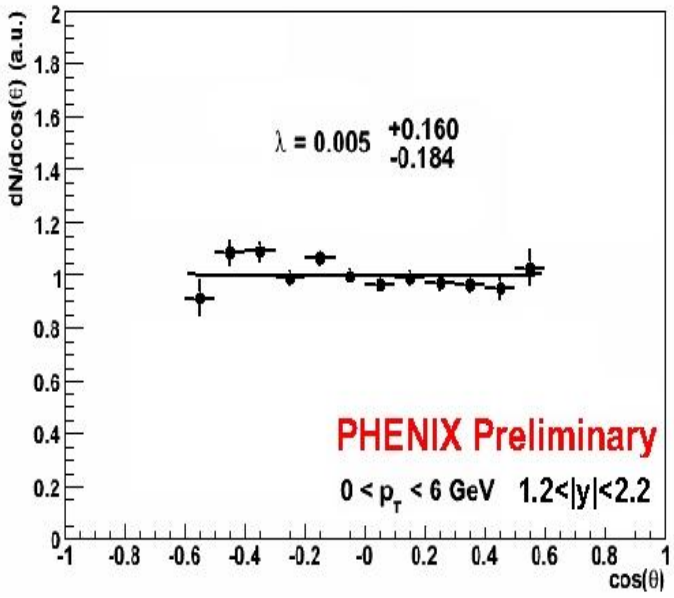

Figure 2.6: Preliminary results from PHENIX: J/ψ polarization in p-p collisions at ... GeV for $p_T < 6$ GeV.

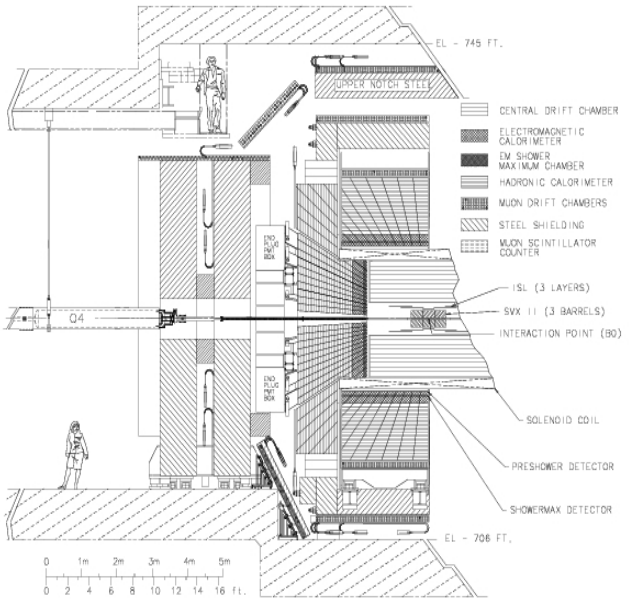

Figure 2.7: The CDF detector at Fermilab Tevatron: left part of the side view.

grated luminosity of about $800pb^{-1}$; results for J/ψ and $\psi(2S)$ can be seen in *Figure 2.8* and they show an evident disagreement with theoretical predictions. In particular NRQCD (which fairly explains the production cross-section dependence on p_T) dramatically fails in predicting the α parameter behaviour for high p_T.

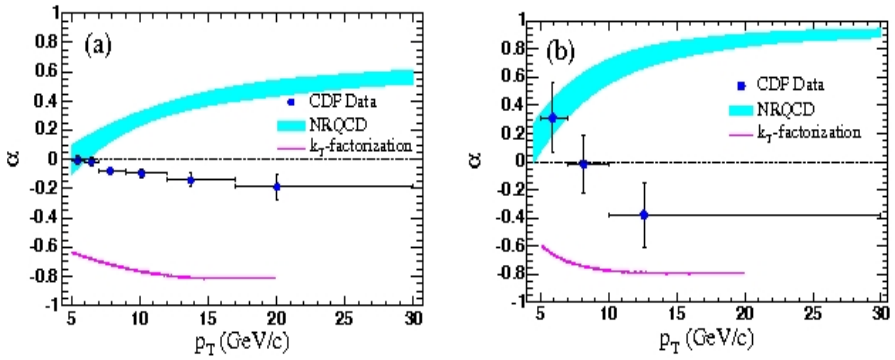

Figure 2.8: CDF Run II results on charmonium polarization in $p\bar{p}$ collisions at $\sqrt{s} = 1.96TeV$: J/ψ data (left) and $\psi(2S)$ data (right). The blue area shows the NRQCD prediction, while the magenta line the k-T factorization expected curve.

Bottomonium polarization analysis have been done with a $77 \pm 3\ pb^{-1}$ sample of $\Upsilon(1S)$ collected in the Run I ($\sqrt{s} = 1.8TeV$) of Tevatron. Results are shown in *Figure 2.9* with the predicted NRQCD calculation (green area): here statistical errors are too wide to allow a definitive conclusion, but the NRQCD prediction seem not to be respected in particular at high p_T. Results on bottomonium from Run II of the Tevatron are not available yet.

2.3.5 D0

Another experiment in which data have been compared with theoretical predictions is D0 at Tevatron (shown in *Figure 2.10*).

This experiment measured the polarization dependence on p_T for a sample of $\Upsilon(1S)$ and $(2S)$ (integrated luminosity of $1.3fb^{-1}$) collected between 2002 and 2006 during the Run II of Tevatron [1]. For what concerns $\Upsilon(1S)$ a strong dependence of α on the p_T is observed and the polarization seems to be longitudinal rather than trasverse in the p_T region 1-12 GeV, while it increases and seems to reach the NRQCD

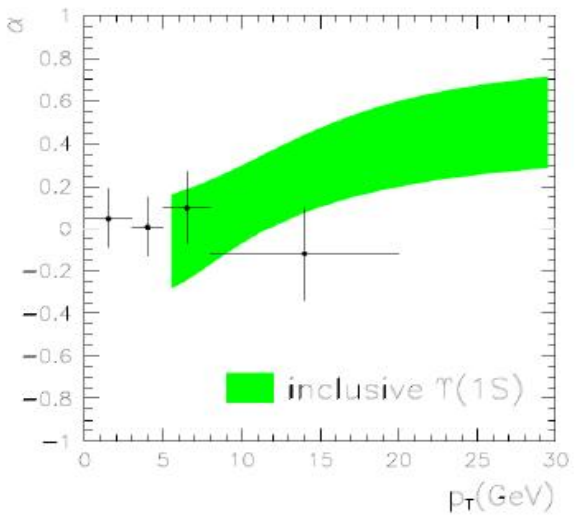

Figure 2.9: CDF Run I results on the $\Upsilon(1S)$ polarization in $p\overline{p}$ collisions at $\sqrt{s} = 1.8TeV$. The green area shows the NRQCD prediction.

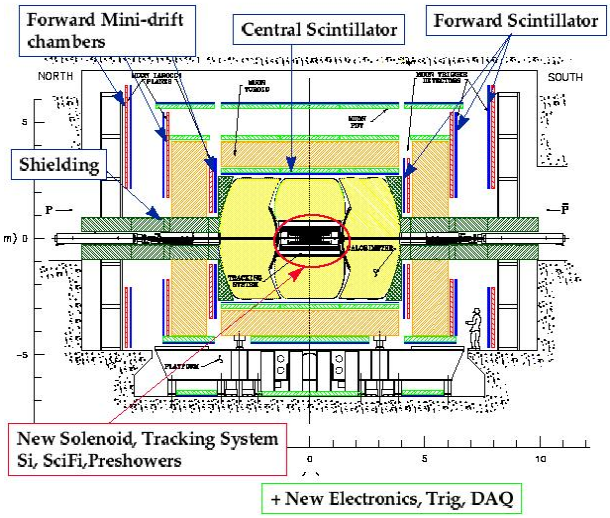

Figure 2.10: D0 detector at Tevatron.

prediction for $p_T > 18$. Data concerning to the $\Upsilon(2S)$ sample, on the contrary, show a fair agreement with NRQCD predictions. It must be noted that D0 and CDF results seem to be at variance, in particular for what concerns Υ polarization at low p_T.

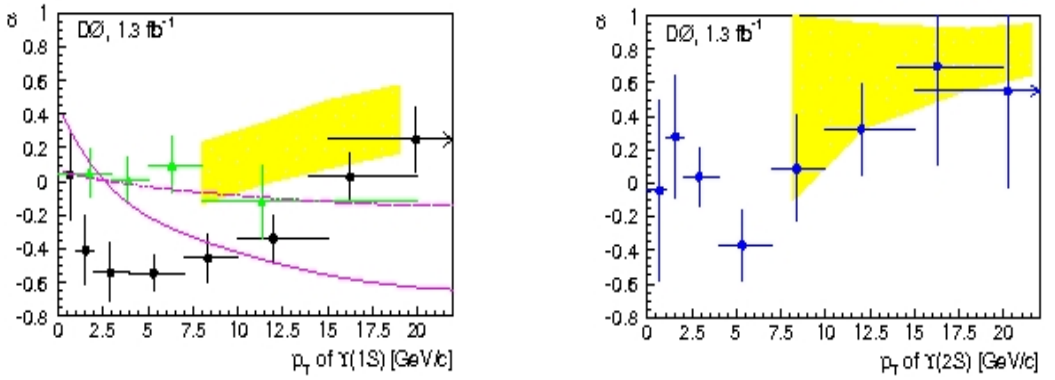

(a) (b)

Figure 2.11: D0 results: polarization of $\Upsilon(1S)$ and $(2S)$ from data collected during Run II of the Fermilab Tevatron (2002-2006). Black dots are data from D0, green triangles are data from CDF, yellow area is the NRQCD prediction, the magenta lines are two limit cases of the k_T-factorization model.

2.3.6 NA60

The NA60 experiment (briefly described is *Section 1.3.3*) measured the J/ψ polarization parameter for In-In collisions at 158 GeV . A sample of $3 \cdot 10^4$ J/ψ has been considered and preliminary results are shown in *Figure 2.12* [31].

Data show a polarization consistent with zero. One interesting thing to be underlined is that the dependance of α with respect to N_{part} tells something about the dependence of the polarization on the medium: these data seem to exclude such a dependence.

To summarize all the results shown before we can say that polarization is a critical issue. Data from CDF and D0 are in general not fitted by NRQCD wich, on the contrary, fits in a satisfactorying way the production cross-section data. From

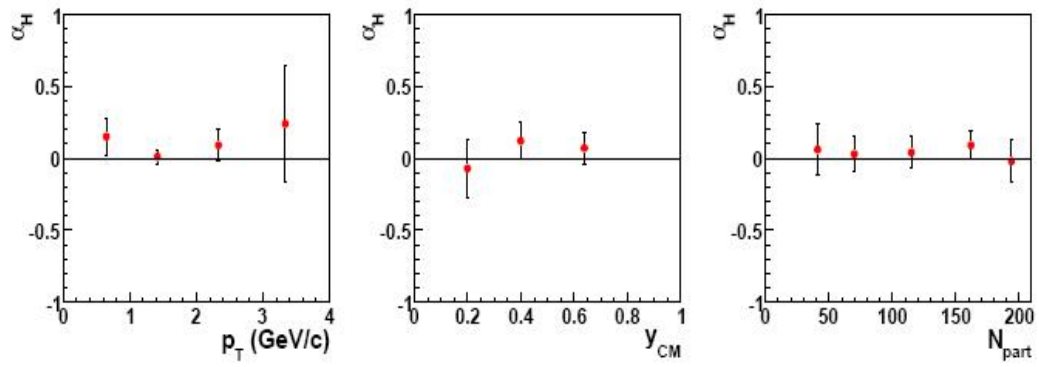

Figure 2.12: NA60 preliminary results on the J/ψ polarization in In-In collisions at 158 GeV: study of the dependence on p_T (left), on y (central) and on N_{part} (right).

this the interest of studying quarkonium polarization at higher energies and with more statistics, in order to have a clearer perspective on production models. The ALICE experiment, thanks to its muon and electron detection capabilities, can detect quarkonium over a large rapidity range in both p-p and Pb-Pb collisions: therefore a polarization study will be very interesting.

Chapter 3

The ALICE experiment at LHC

The ALICE experiment was first proposed as a central detector in the 1993 Letter of Intent (LoI), and later complemented by an additional forward muon spectrometer designed in 1995. It is a general-purpose heavy-ion experiment, sensitive to the majority of known observables (including hadrons, electrons, muons and photons). ALICE was designed in order to measure the flavor content and phase-space distribution, event-by-event, for a large number of particles whose momenta and masses are of the order of the typical energy scale involved (temperature $\sim \Lambda_{QCD} \sim 200$ MeV). The experiment will be able to cope with the highest particle multiplicities anticipated for PbPb reactions (up to 8000 per rapidity unit).

In the present chapter an overview on the LHC accelerator and on the ALICE detector can be found, as well as a more detailed description of the muon spectrometer. Finally the analysis framework of the experiment is descripted.

3.1 The Large Hadron Collider (LHC)

With a circumference of 27 km, the Large Hadron Collider at CERN is the largest collider experiment in the world. It is housed in the tunnel of the previous Large Electron Positron collider, at a depth between 50 and 175 m underground. It will serve as both a proton and ion collider.

The nominal luminosity for p-p collisions is of $10^{34} s^{-1} cm^{-2}$, while for Pb-Pb collisions it is about $10^{27} s^{-1} cm^{-2}$. The PS and SPS rings will be used as injectors for the machine (see *Figure 3.1*); in particular the SPS will inject protons in the LHC

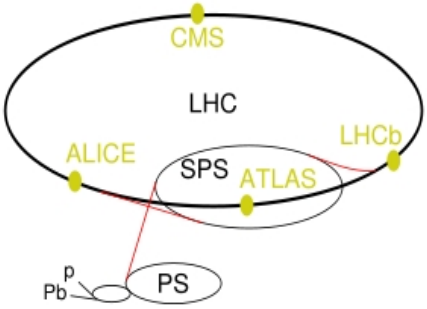

Figure 3.1: The Large Hadron Collider scheme: injectors and main ring.

ring with an energy of 450 GeV. The beams will be accelerated in two separate rings, with intersections corresponding to the experiments.

The LHC official schedule includes:

- regular p-p runs at $\sqrt{s} = 14TeV$ (9 months/year $\simeq$ 10^7 s/year);
- 1$\div$2 years Pb-Pb runs at $\sqrt{s} = 5.5TeV$ per nucleon pair at nominal luminosity (1 month/year $\simeq$ 10^6 s/year);
- 1 year hybrid collisions (p-Pb at $\sqrt{s} = 8.8TeV$ per nucleon pair, d-Pb or α-Pb);
- 1 year Ar-Ar.

The schedule for the second phase of operation has not been fixed yet, since it will depend on the outcome of the above program.

The main experiments running at the LHC will be:

- A Toroidal LArge Solenoid (ATLAS): a large general purpose experiment whose main goal is the search for the Higgs boson;
- Compact Muon Solenoid (CMS): same as ATLAS;
- LHC-beauty (LHCb): an experiment designed to study CP violation in the sector of b-hadrons;
- A Large Ion Collider Experiment (ALICE): the only LHC experiment dedicated to heavy ion physics;

- Total Cross Section, Elastic Scattering and Diffraction Dissociation (TOTEM): a detector which will measure total and elastic cross sections and diffractive processes; shares the interaction point with CMS;

- LHC-forward (LHC-f): an experiment designed to measure the energy and number of forward neutral pions produced in the collisions; shares the interaction point with ATLAS.

3.2 ALICE detector: overview

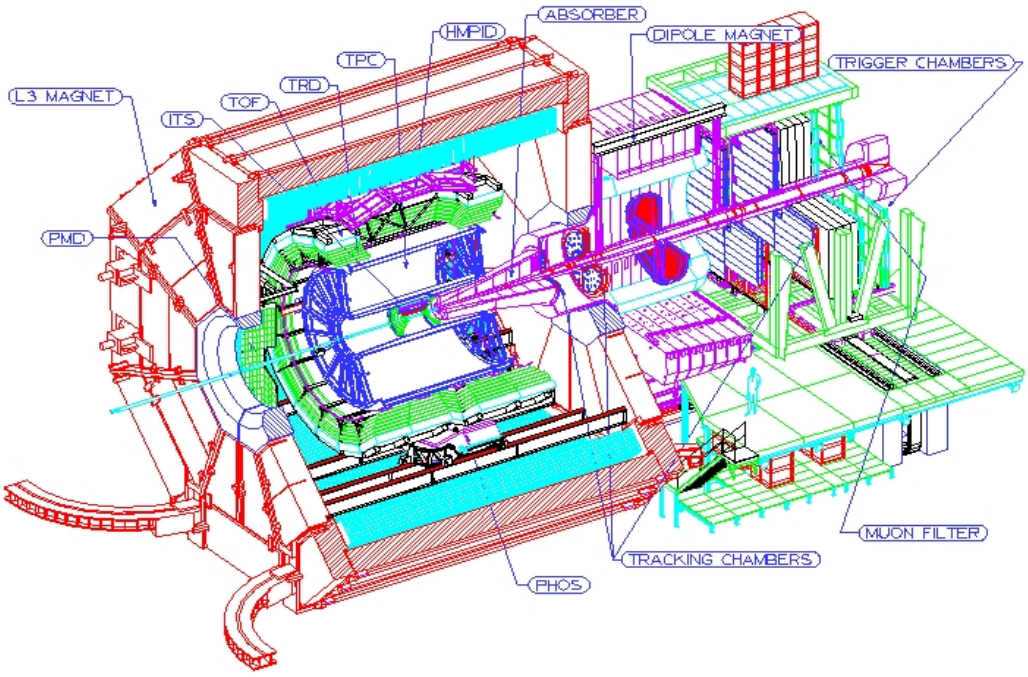

Figure 3.2: Longitudinal view of the ALICE detector

ALICE detectors, showed in *Figure 3.2*, can roughly be divided into three parts: the central barrel with the tracking detectors, the forward one dedicated to particles with large rapidity and the one aimed to PID (Particle IDentification).
The central system includes, from the interaction vertex to the outside, six layers of high-resolution silicon detectors (Inner Tracking System—ITS), the main tracking system of the experiment (Time-Projection Chamber—TPC), a transition ra-

diation detector for electron identification (Transition-Radiation Detector—TRD), and a particle identification array (Time Of Flight—TOF). The central system is complemented by two small-area detectors: an array of ring-imaging Cherenkov detectors ($|\eta| \leq 0.6, 57.6^\circ$ azimuthal coverage) for the identification of high-momentum particles (High-Momentum Particle Identification Detector—HMPID), and an electromagnetic calorimeter ($|\eta| \leq 0.12$, 100° azimuthal coverage) consisting of arrays of high density crystals (PHOton Spectrometer—PHOS).
The large rapidity systems include a muon spectrometer ($-4.0 \leq \eta \leq -2.4$, on the RB26 side of the solenoid), a photon counting detector (Photon Multiplicity Detector—PMD, on the opposite side), an ensemble of multiplicity detectors (Forward Multiplicity Detector—FMD) covering the large rapidity region (up to $\eta = 5.1$). A system of scintillators and quartz counters (T0 and V0) will provide fast trigger signals, and two sets of neutron and hadron calorimeters, located at 0° and about 116 m away from the interaction vertex, will measure the impact parameter (Zero-Degree Calorimeter—ZDC). An absorber positioned very close to the vertex shields the muon spectrometer, which consists of a dipole magnet, five tracking stations, an iron wall (muon filter) to absorb remaining hadrons, and two trigger stations behind the muon filter.

3.2.1 Magnets

The ALICE experiment uses two large magnets.
The central part of the detector is enclosed in the solenoid magnet constructed for the L3 experiment at LEP, with an internal length of 12 m and a radius of 5 m. The nominal field of the solenoid is 0.5 T. The diameter of the axial holes in the magnet 'doors' has been reduced in order to improve the magnetic field homogeneity in the volume of the TPC. An improvement by a factor two has been achieved compared to the L3 situation. The field variations in the volume of the detectors, up to 2.5 m in radius and $\pm$ 2.5 m along the axis around the centre, are below 2% of the nominal field value.
A large warm dipole magnet with resistive coils and a horizontal field perpendicular to the beam axis is used for the muon spectrometer (see *Section 3.3*). The field integral in the forward direction is 3 T m.
The polarity of the magnetic fields in both magnets can be reversed within a short

time.

3.2.2 Inner Tracking System (ITS)

The main purposes of the ITS are the detection of the primary and secondary vertices (hyperons and charm) and the stand-alone track finding of low p_T charged particles, down to p_T of $\sim$ 20 MeV/c for electrons. Moreover it can be used to improve the momentum resolution at high momenta, to reconstruct low energy particles and to identify them via energy loss.

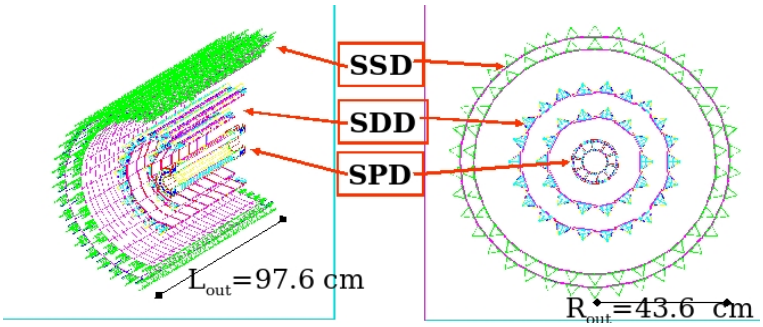

Figure 3.3: The ITS scheme

The system consists of six cylindrical layers of coordinate-sensitive detectors. The granularity required for the innermost planes, given the expected high multiplicity of charged particle tracks, can only be achieved with silicon micro-pattern detectors with two-dimensional readout, such as Silicon Pixel Detectors (SPDs) and Silicon Drift Detectors (SDDs). In particular silicon pixel detectors are used in the first two layers, silicon drift detectors in the third and fourth layers and, in the fith and sixth, where requirements in term of granularity are less stringent, strip detectors are used.

3.2.3 Time-Projection Chamber (TPC)

The TPC (see *Figure 3.4*) is the main tracking detector of the central barrel. Its function is to provide track finding (efficiency larger than 90%), charged particle momentum measurement (resolution better than 2.5% for electrons with momentum of about 4 GeV/c), particle identification (dE/dx resolution better than 10%), and two-track separation (resolution in relative momentum below 5 MeV/c) in the region $p_{\mathrm{T}} < 10 GeV/c$ and pseudo-rapidity $|\eta| < 0.9$.

The TPC is cylindrical in shape with an active gas volume that ranges from about 85 cm to 250 cm in the radial direction, and has a length of 500 cm along the beam direction. A high voltage (HV) electrode is located at its axial center, which has been aligned to the interaction point, dividing the gas volume in two symmetric drift regions of 250 cm length. The HV electrode, which consists of an aluminized stretched Mylar foil, and two opposite axial potential degraders create a highly uniform electrostatic field in the two drift regions.

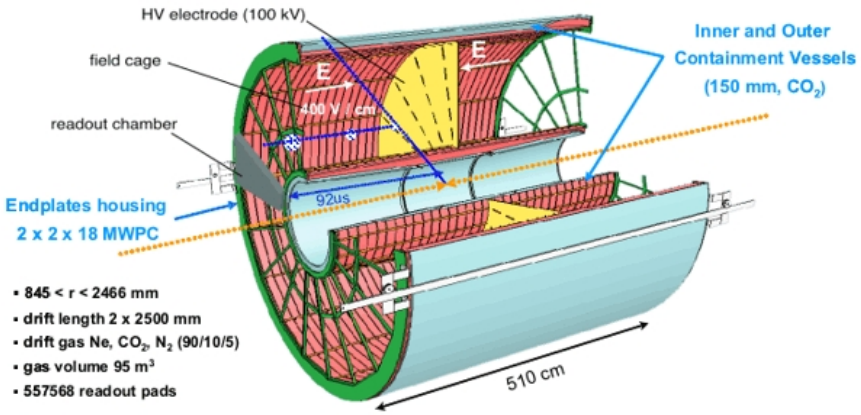

Figure 3.4: The TPC detector layout

The ionization trace moves at constant velocity to either of the two end-plates. Each end-plate, segmented into 18 trapezoidal sectors and equipped with multi-wire proportional chambers with cathode pad readout covering an overall active area of $32.5m^2$, will detect the fundamental properties of the ionization trace (3D image and ionization density).

The requirements of good momentum resolution and high rate capability call for a drift gas with low diffusion, low Z and large ion mobility. Extensive investigation of different gas mixtures led originally to the choice of the mixture $90\%Ne - 10\%CO_2$. More recently it was proposed to add $5\%N_2$ to the mixture, which turned out to provide higher gas gain stability and a good influence on the drift velocity. Both gas mixtures, however, require a high drift field (400 V/cm) to secure an acceptable drift time (88μs and 92μs respectively).

3.2.4 High-Momentum Particle Identification Detector (HMPID)

The ALICE HMPID is based on proximity focusing Ring Imaging Cherenkov (RICH) counters and consists of seven modules mounted in an independent support cradle, which has been fixed to the space frame, at the two o'clock position.

Cherenkov photons, emitted when a fast charged particle traverses the 15 mm thick layer of liquid C_6F_{14} (perfluorohexane), are detected by a photon counter, which exploits the novel technology of a thin layer of CsI deposited onto the pad cathode of a multi-wire proportional chamber (MWPC). The HMPID detector, with its surface of about 12 m^2, represents the largest scale application of this technique.

The Cherenkov photons refracts out of the liquid radiator and reach the CsI-coated pad cathode, located at a suitable distance (the 'proximity gap') that allows the contribution of the geometrical aberration to the Cherenkov angle resolution to be reduced. The electrons released by ionizing particles in the proximity gap, filled with CH_4, are prevented from entering the MWPC sensitive volume by a positive polarization of the 'collection' electrode close to the radiator.

3.2.5 Transition-Radiation Detector (TRD)

The TRD detector fills the radial space between the TPC and the TOF. It is constituted by a total of 540 detector modules, each consisting of a radiator and a multi-wire proportional readout chamber, together with its front-end electronic. The detector will provide electron identification for momenta grater than 1 GeV/c, where the pion rejection capability through energy-loss measurement in the TPC is no longer sufficient. Such identification, in conjunction with ITS, will be used in order to measure open charm and open beauty, as well as light and heavy vector mesons produced in the collisions. Moreover, the combined use of TRD and ITS data will allow to separate the directly produced J/ψ mesons from those coming from B-decay.

3.2.6 Time Of Flight (TOF)

The TOF detector in ALICE is dedicated to charged particle identification over a very large part of the phase space. The basic physics goals of the ALICE experiment demand a Time of Flight detector with outstanding characteristics:

- The TOF rapidity acceptance has to be large enough to cover the full central

acceptance of ALICE, in order to allow a significant study of the observables of interest on a Event-by-Event basis. This implies that a large number of hadrons of average momenta $\sim 1\ GeV$ should be detected. More precisely, the TOF detector should cover the hadron momentum range from about 0.5 GeV/c (upper limit for dE/dx measurements in both the ITS and TPC detectors for kaon/pion separation) to about 2.5 GeV/c (statistics limit in single events).

- The TOF intrinsic time resolution must be well below 100 ps; an 'overall' time resolution of 120 ps, including all other sources of timing errors, would guarantee a 3 sigma separation up to 1.9 GeV/c for kaon/pion and up to 3.2 GeV/c for proton/kaon.

Since a large area (150 square meters) has to be covered, a gaseous detector is the only choice and in particular it has been proved that the best solution for the Time of Flight detector is the Multigap Resistive Plate Chamber. The key aspect of this technology is that the electric field is high and uniform over the whole sensitive gaseous volume of the detector. Any ionisation produced by a through-going charged particle will immediately start a gas avalanche process which will eventually generate the observed signals on the pick-up electrodes.

3.2.7 PHOton Spectrometer (PHOS)

The PHOS is an electromagnetic calorimeter designed to search for direct photons, but it can also detect γ coming from π^0 and η decays at the highest momenta, where the momentum resolution is one order of magnitude better than for charged particles measured in the tracking detectors. The study of the high momentum particles spectrum is extremely useful because it gives information about the propagation of jets in the dense medium created during the collision ("jet quencing").

In addition to photons, the PHOS also responds to charged hadrons and to neutral particles such as K_L^0, n and $\overline{n}$. To reject these particles a charged-particle veto detector (CPV) placed in front of the calorimeter is used together with a cut on the shower width and on the time of flight for neutral particles. The calorimeter is placed at 4.6 m from the beam axis, covers the pseudorapidity region $|\eta| \leq 0.12$ and has an area of 8 m^2.

3.2.8 Forward Multiplicity Detector (FMD)

The purpose of the FMD is to measure $dN/d\eta$ in the rapidity region outside the central acceptance and to provide information for the trigger system in a very short time.
The FMD is a silicon detector segmented into seven disks which surround the beam pipe at distances of between 42 and 225 cm from the vertex. Together they will cover the pseudorapidity range from -3.4 to -1.7 on the muon arm side and from 1.7 to 5.1 on the opposite hemisphere. It is designed in order to measure charged particle multiplicities from tens (in pp runs) to thousands (Pb-Pb runs) per unit of pseudorapidity.

3.2.9 Poton Multiplicity Detector (PMD)

The PMD is a preshower detector that measures the multiplicity and spatial distribution of photons in order to provide estimates of the transverse electromagnetic energy and the reaction plane.
It consists of two identical planes of proportional chambers with a $3X_0$ thick lead converter in between. It has been installed at 350 cm from the interaction point, on the opposite side of the muon spectrometer, covering the region $2.3 < \eta < 3.5$, in order to minimize the effect of upstream material such as the beam pipe and the structural component of TPC and ITS.

3.2.10 Muon Spectrometer

For a detailed description of the dimuon spectrometer see *Section 3.3*.

3.2.11 ElectroMagnetic Celorimeter (EMCal)

The main physics motivation for the EMCal is to improve the ALICE performances for an extensive study of "jet quencing": in fact the EMCal extends the ALICE p_T capabilities for jets, direct photons and electrons from heavy-flavor decays.
The detector contains several modules each consisting of sampling calorimeters made of alternating layers of Pb and polystyrene, which is scintillating material. The EMCal covers the pseudo-rapidity range $-0.7 \leq \eta \leq 0.7$. It is positioned to provide

partial back-to-back coverage with the PHOS and its nominal acceptance is about 25% of the TPC acceptance.

3.2.12 Zero-Degree Calorimeter (ZDC)

The main aim of the ZDC is the estimate of the collision geometry through the measurement of the non-interacting beam nucleons (the "spectators"). There are four calorimeters, two for neutrons and two for protons, placed at 116 m from the interaction point, where the distance between the beam pipes ($\sim 8\ cm$) allows the insertion of a detector (the neutron calorimeter). At this distance, spectator protons are spatially separated from neutrons from the magnetic elements of the LHC beam line.

The neutron detector is made up of a tungsten alloy, while the proton one is costituted of brass. Both calorimeters have quartz fibers as the active material instead of the conventional scintillating ones.

3.2.13 T0 and V0 detectors

The T0 detector, made of 24 Cerenkov radiators, generates the T0 signal for the TOF with a precision of $\sim 50ps$, measures a rough vertex position, provides a first level trigger and helps to dicriminate against beam-gas interaction.
Te V0 detector, consisting of scintillators, provides a minimum bias trigger for the central barrel detectors and can be used as a centrality indicator.
Both T0 and V0 consist of two modules installed on each side of the interaction point.

3.3 The Muon Spectrometer

The muon spectrometer (showed in *Figure 3.5*) was specifically designed in order to detect heavy quarkonia in the muon pairs decay channel. As the primary interest is on ψ and Υ resonances directly produced in the collision, it is important to measure charmonia and bottomonia at low p_T, where the contribution from B and D mesons decay is lower.

Muon identification in the LHC environment is only feasible for muon momenta above $\sim$ 4 GeV, because of the amount of absorber material required to reduce the

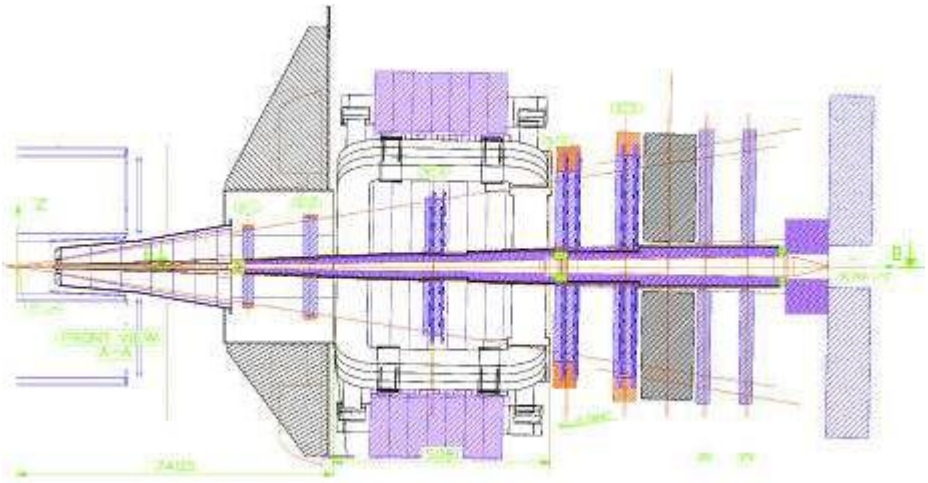

Figure 3.5: Sideview of the muon spectrometer layout

flux of hadrons. Hence the important measurement of low p_T quarkonium is possible only at small angles in the forward region, where the muons are Lorentz-boosted. Moreover, owing to the higher momenta of hadrons at forward rapidity and the corresponding lower decay probability, the background of decay muons is also reduced in the forward region. These are the reasons that led the design criteria of the detector.

The angular acceptance of the muon spectrometer goes from 171° to 178° ($-4 < \eta < -2.5$). Its mass resolution (determined by angle and energy-loss fluctuations in the front absorber, multiple scattering in the tracking chambers, spatial resolution, number and position of the tracking planes and the magnetic field integral of the muon magnet) is better than 100 MeV at around 10 GeV, sufficient to separate all resonence states.

The detector consists of a composite absorber starting 90 cm from the vertex, a large dipole magnet with 3 Tm field integral placed outside the L3 magnet, and 10 planes of thin, high-granularity tracking stations. The picture is completed by a second absorber, made of iron and acting as a muon filter, and four more detector planes, used for triggering. The spectrometer is shielded throughout its length by a dense absorber tube, of about 60 cm outer diameter, which surrounds the pipe.

Beside the heavy quarkonia detection, the ALICE muon spectrometer will provide a spectrum of the Φ meson and, in conjunction with TRD, will be able to study the

heavy flavor production in the region $-2.5 < \eta < -1$, owing to the measurement of the $e - \mu$ coincidences.

3.3.1 Absorbers

The muon arm contains three absorber sections:

- the front absorber in the acceptance region ($\sim 10\lambda_{int}$);
- the beam shield surrounding the beam pipe;
- the muon filter between the tracking and the trigger chambers ($\sim 7.2\lambda_{int}$).

The front absorber (total length of 4.13 cm) has the double task of attenuating the particle flux into the muon spectrometer by at least two orders of magnitude and of decreasing the muon background by limiting the free path for primary $\pi, K \rightarrow \mu$ decays. The minimal distance to the interaction point (90 cm) is imposed by the dimension of the inner tracking system and the position of the mutiplicity counters.

The front section consists of dense low-Z materials to limit multiple scattering, while the rear one contains alternating layers of neutron moderator and absorber and high-Z material to shield against neutrons and photons.
The use of a very dense material at the end of the absorber has an important consequence for the tracking. Since the multiple scattering in this layer is large, whereas the distance to the first tracking chamber is small, the muon production angle is best defined by combining the position measurement in the first chamber with the position of the interaction vertex, determined by the inner tracking system.

Outside the muon arm acceptance, a tungsten cone at $\theta < 2^\circ$ absorbs particles emanating from the beam pipe, and lead is employed at $\theta > 10^\circ$ to reduce the particle load in the TPC.

The small-angle beam shield consists of dense material encased in a 4 cm thick stainless steel tube. Its outer envelope is "pencil shaped", i.e. it follows an angle of 2° until it reaches an outer radius of 30 cm and then stays constant up to the end of the spectrometer. The 30 cm radius prevents acceptance losses by taking into account the bending of tracks in the dipole field.

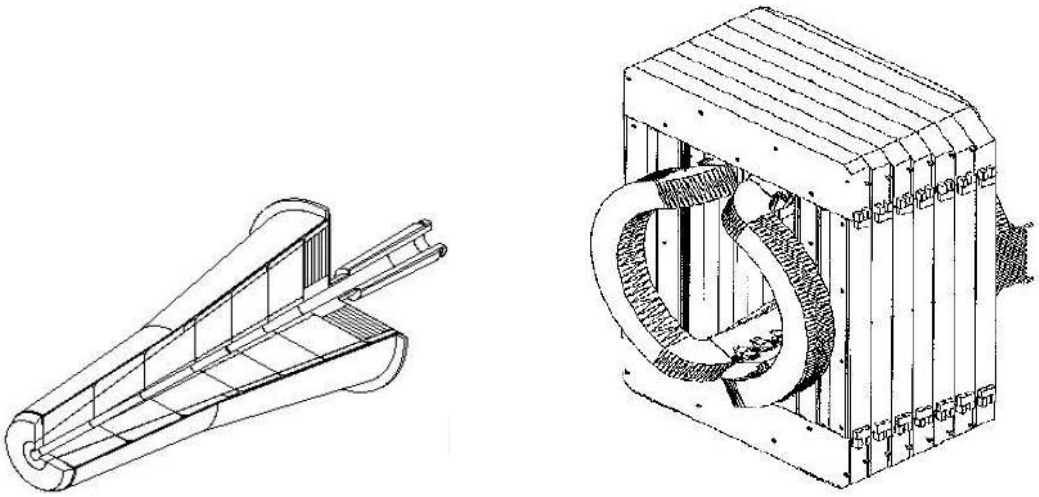

(a) (b)

Figure 3.6: Muon Spectrometer: the front absorber (3.6(a)) and the dipole magnet (3.6(b)).

The muon filter consists of a $5.6 \times 5.6 \times 1.2\ m^3$ iron wall, located at z= 15 m between the last tracking and the first triggering plane. The hit rate in the trigger chambers is mainly due to surface emissions of soft particles from the beam shieldin and the backside of the muon filter.

3.3.2 Magnetic dipole

The size and bending strength of the muon spectrometer magnet are defined by the requirements on mass resolution and geometrical acceptance. The magnet has to cover the pseudorapidity range $-4 < \eta < -2.5$, corresponding to an angular acceptance of $171° < \theta < 178°$.

Given the reduced requirements on size and magnetic field ($B_{nom} \sim 0.7T$), it is not necessary to use a superconductiong magnet. It was therefore chosen a window-fram warm magnet equipped with resistive coils and arranged so as to produce a magnetic field in the horizontal direction, along the x-axis (orizontal direction, center of LHC versus). With its integral magnetic field of 3 Tm, the dipole will be able to bend the muons along the y-axis (vertical direction, up versus) and will allow a mass resolution better than 100 MeV, enough to separate the bottomonium states. The

magnet is placed directly adjacent to the ALICE L3 magnet.

3.3.3 Tracking Chambers

The muon tracking system is composed of 5 stations, each consisting of 2 layers of multi-wire chambers. Two of them are located in front of the muon magnet, two others behind and one in its center. Each chamber is read out by cathode planes in two orthogonal projections (X-Y) to provide two dimensional hit information.
The two stations before and after the dipole magnet measure the corresponding track angles and the station located inside the magnet adds sagitta information. This layout provides redundant information and can operate even if one of the ten station planes doesn't work. The chambers are arranged in a projective geometry and are slightly larger than the acceptance of the spectrometer to account for bending in the magnetic field. The total sensitive surface is about $100m^2$.

In order to achieve a mass resolution better than 100 MeV, the tracking chambers have to meet the following requirements:

- spatial resolution $< 100\mu m$ to achieve a spatial momentum resolution of $\Delta p/p < 1\%$;
- resolution of $\sim 2mm$ in the non-bending plane to reconstruct the angle of the muons and to allow an efficient pattern recognition;
- average material thickness of each sensitive plane of about 2-3 % of X_0;
- efficiently operativity at hit densities of up to $3 \times 10^{-2} cm^{-2}$, as expected in the first station;
- low sensitivity to photon and neutron backgrounds.

Cathode Pad Chambers (CPC) and Cathode Strip Chambers (CSC) are the best suited segmentation configurations for the muon arm. They, in fact, allow a fine segmentation of the cathode plane which, in addiction, can be continuously varied across the chamber area. The channel occupancy can thus be kept constant by adapting the pad or strip size to the local particle density.

Pads are used in the innermost region, while ar large radii strips are adopted. The position resolution has been evaluated with three different methods (center of

gravity, ratio of charges on adjacent pads and fitting to charge distribution with a realistic function), giving a result of about 50 μm.

3.3.4 Trigger Chambers

In central Pb-Pb collisions, about eight low-p_T muons from π and K decays are expected to be detected per event in the spectrometer. To reduce to an acceptable level the probability of triggering on events where those low-p_T muons are not accompanied by the high-p_T ones, emitted in the decay of heavy quarkonia, a p_T cut has to be applied at the trigger level on each individual muon.

A dimuon trigger signal is issued when at least two tracks above a predefined p_T threshold are detected in an event. According to simulation results, a "low"-p_T cut (1 GeV/c) will be used for J/ψ and a "high" one (2 GeV/c) for Υ selection.

The trigger is performed by two trigger stations, each consisting of two single gap Resistive Plate Chamber (RPC), placed behind the muon filter. RPCs match all the requirements concerning position resolution, fast response and low sensitivity to neutron and photon background.

Within ALICE, two trigger levels are foreseen for the muon spectrometer. A first level trigger (L0) rejects most of the low-p_T muons, below the defined threshold, which are essentially due to π and K decays. Some fast barrel detectors, like the pixel planes of the ITS, are read in coincidence. The decision to collect these events has to be available locally after a fixed latency of less than 1 μs in order to be distributed to the muon tracking chambers. This is achieved by using dedicated trigger electronics which work independently and in parallel to find muon candidates: two muons above a p_T threshold are required to give a L0 trigger signal.
The high level trigger (HLT) is more selective by sharpening the transverse momentum cut of the muon pairs. This trigger, carried out by online computer processing, will reduce the need in bandwidth and data storage by a factor of four to five.

The first level trigger is based on a transverse momentum cut in order to reduce the huge rate of low-p_T muons from π and K decays. It requires a coincidence between the two trigger stations in which impact points must lie within a "road", whose width depends on the magnetic field and on the desired momentum threshold. Each hit in the first trigger station is combined with any hit inside a variable search area in the second station. Moreover, an approximate pointing towards the vertex is

required in the non-bending plane.

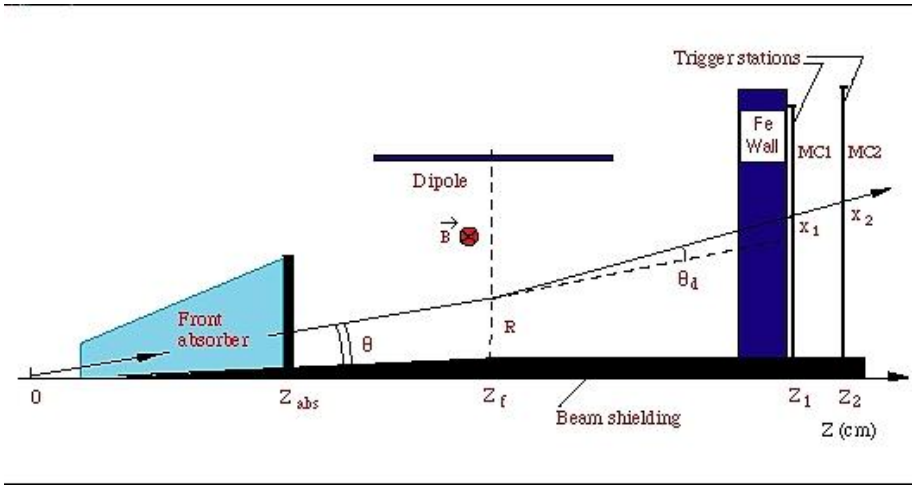

Figure 3.7: The muon trigger scheme

In practice such a p_T cut is performed approximately, knowing only the positions (in the bending plane) detected in the two trigger stations. Given an x_1 value in the first station, a band in the second station can be determined according to the p_T limit considered. If the particle falls outside that region it is rejected (see *Figure 3.7*).

In the high level trigger, the muon p_T is calculated by using the information of the last two tracking chambers. In this way the accurancy in the lepton position measurement is enhanced, thus providing a better determination of the transverse momentum.

The two main sources of background in the trigger chambers are muons from particle decays and low-energy particles leaking out of the absorber and beam shield. In fact most of the soft background is due to electrons belonging to the latter category. The rest is from γ and neutrons interactions in the chamber material itself. These particles create random hits which are not correlated between the chamber planes. In addiction, the background is spread out in time on a μs time scale and can be partially rejected (the time interval that elapses between the detection of the fastest and the lowest muon is $\leq 5ns$).

The RPCs are perfectly suited for background rejection and muons detection owing to their characteristics that can be summarized as:

- fast response time ($\sim$ 2 ns);
- good time resolution ($\sigma t \sim 1ns$);
- high efficiency;
- spatial resolution $< 1cm$;
- neutron sensitivity of $\sim 3 \times 10^{-3}$ and $< 10^{-4}$ for 1 MeV and thermal neutrons respectively;
- gamma sensitivity $\leq 10^{-2}$;
- low cost and industrial production potential.

3.3.5 Track recontruction

The muon arm was specifically designed to measure low p_T quarkonia with a mass resolution better than 100 MeV. The mass resolution is essentially determined by the precision reached in the measurement of the angle between the two muons and of their momenta. Unfortunately behind the absorber the angular information is almost lost, because of the multiple scattering.

The reconstruction of the angle between the two muon tracks makes use of the event vertex, measured with high precision by the Si pixel layers of the ITS. Therefore, the angular precision is mainly determined by the lateral displacement of the muon tracks in the absorber and not so much by the scattering angle.

The momentum resolution depends on three main contributions: measurement precision of the tracking chambers, multiple scattering inside the tracking system and energy-loss fluctuations in the absorber. The relative importance of these contributions depends on the track momentum.

The tracking starts with a matching in the two nearby detection planes of each station. All hits of the second plane laying in a road defined by the vertex position and the hit position in the first plane, are kept to feed the track-finding algorithm. This one starts from the last two muon stations where hit densities are more favorable. Higher momentum tracks are processed first, as they have the smaller extrapolation errors from multiple scattering and from track curvature.
In a first step vectors are extrapolated from Station 4 to Station 5 and conversely in

order to initiate the track-finding procedure with a straight line behind the magnet. In a second step tracks are extrapolated to the interaction point through the magnetic field and the nearest vector (or single hit) found in the neighboring tracking station is added to the track. A track is validated if at least three hits (out of four possible) are found in the detector planes behind the dipole magnet and at least one hit (out of two) in the station located inside the magnet and in the chambers in front of the magnet.
The procedure stops when the next candidate has an extimated momentum of below 3 GeV/c, since such muons come essentially from background sources.

3.4 The ALICE Software Framework

The ALICE Off-line Project has started developing the software framework in 1998. The decision was taken at the time to build the simulation tool for the Technical Design Reports of the ALICE detector using the OO programming technique and C++ as an implementation language.
This lead to the choice of ROOT as framework and GEANT 3.21 as simulation code. A prototype was quickly built and put in production. The experience with this was positive, and in November 1998 the ALICE Off-line project adopted ROOT as the official framework of ALICE Off-line.

AliRoot is the name ALICE Off-line framework for simulation, reconstruction and analysis. It uses the ROOT system as a foundation on which the framework and all applications are built. Except for large existing libraries, such as GEANT3.21 and Jetset, and some remaining legacy code, this framework is based on the Object Oriented programming paradigm, and it is written in C++. The ROOT system is now being interfaced with the emerging Grid middle-ware in general and, in particular, with the ALICE-developed AliEn system. In conjunction with the PROOF (Parallel ROOT Facility) system, which extends the ROOT capability on parallel computing systems and clusters, this framework provides a distributed parallel computing platform for large-scale production and analysis.

In this section a description of the main features of the offline framework is carried out.

3.4.1 Overview of the AliRoot Offline framework

The AliRoot design architecture is schematically shown in *Figure 3.8*. The STEER module provides steering, run management, interface classes, and base classes. The detector code is stored in independent modules that contain the code for simulation and reconstruction while the analysis code is progressively added. Detector response simulation can be performed via different transport codes like GEANT3, GEANT4, and FLUKA.

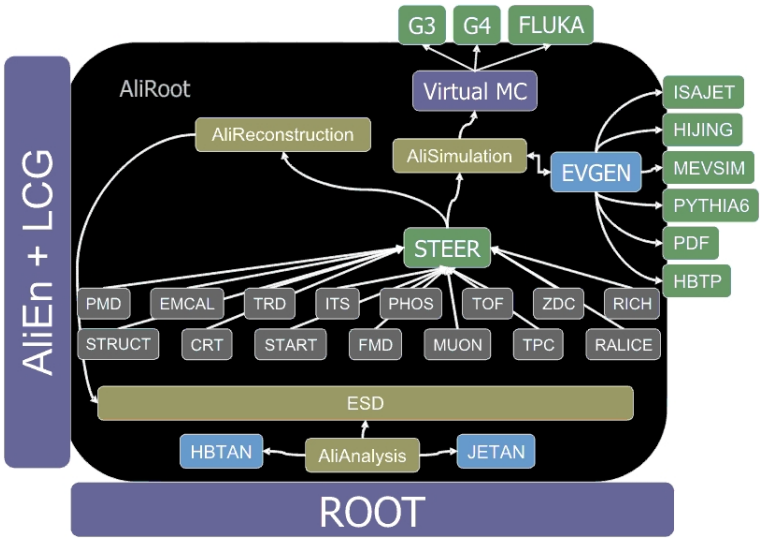

Figure 3.8: AliRoot layout.

Simulation

An event generator produces a set of "particles" with their momenta. The set of particles, where one maintains the production history (in form of mother-daughter relationship and production vertex) forms the kinematic tree.
The transport package brings the particles through the set of detectors, and produce *hits*, which in ALICE terminology means energy deposition at given point. The hits contain also information ("track labels") about the particles that have generated them. There is one main exception, namely the calorimeter (PHOS and EMCAL) hits, where a hit is the energy deposition in the whole detecting element volume. This happens because inside these detectors the particle is completely stopped. Fur-

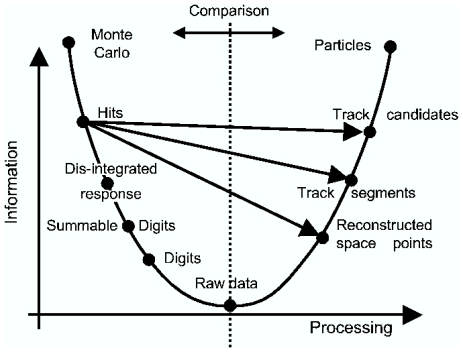

Figure 3.9: Parabolic path of data flow.

thermore in some detectors the energy of the hit is used only for comparison with a given threshold, for example in TOF and ITS pixel layers. These are in fact "digital" detector in the sense that they are requested only for an On-Off response , depending on the threshold overcoming.

At the next step the detector response is taken into account, and the hits are transformed into *digits*. As it was explained above, the hits are closely related to the tracks which generated them. The transition from hits/tracks to digits/detectors is shown in *Figure 3.9* as the left part of the parabolic path. There are two types of digits: *summable digits*, where one uses low thresholds and the result is additive, and *digits*, where the real thresholds are used, and the result is similar to what one would get in the real data taking. In some sense the *summable digits* are precursors of the *digits*. The noise simulation is activated when *digits* are produced. There are two differences between the *digits* and the *raw* data format produced by the detector: firstly, the information about the Monte Carlo particle generating the digit is kept, and secondly, the raw data are stored in binary format as "payload" in a ROOT structure, while the digits are stored in ROOT classes.

Two conversion chains are provided in AliRoot: *hits* $\rightarrow$ *summable digits* $\rightarrow$ *digits*, and *hits* $\rightarrow$ *digits*. The summable digits are used for the so called "event merging", where a signal event is embedded in a signal-free underlying event. This technique is widely used in heavy-ion physics and allows to reuse the underlying events with substantial economy of computing resources. Optionally it is possible to perform the conversion *digits* $\rightarrow$ *raw data*, which is used to estimate the expected data size, to evaluate the high level trigger algorithms, and to carry on the so called computing

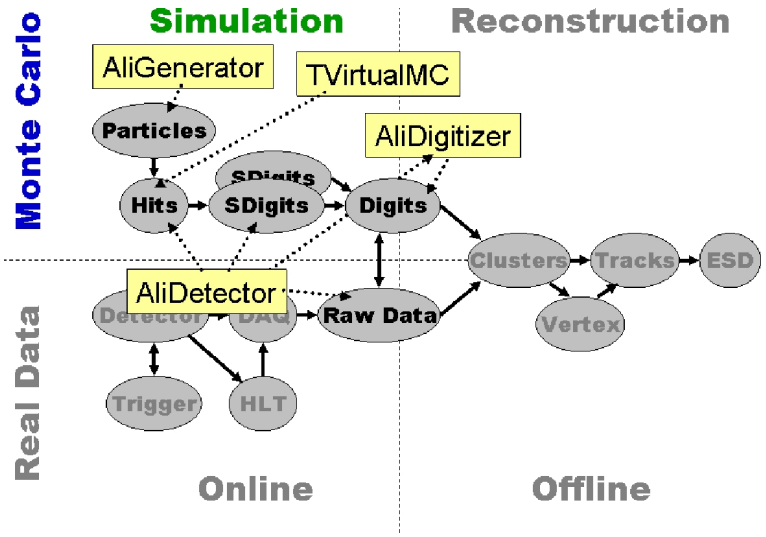

Figure 3.10: *Simulation framework.*

data challenges.

The whole simulation process, represented in *Figure 3.10*, includes the following steps regardless of the detector response simulation package in use:

- **Event generation of final-state particles:** The collision is simulated by a physics generator code (since they predict different scenarios for the same aspect, one has many generators like PHYTHIA, HIJING and FLUKA) or a parameterisation (with the class `AliGenParam`) of the kinematical variables and the final-state particles are fed to the transport program.

- **Particle tracking:** The particles emerging from the interaction of the beam particles are transported in the material of the detector, simulating their interaction with it, and the energy deposition that generates the detector response (hits).

- **Signal generation and detector response:** During this phase the detector response is generated from the energy deposition of the particles traversing it. This is the ideal detector response, before the conversion to digital signal and the formatting of the front-end electronics is applied.

- **Digitisation:** The detector response is digitised and formatted according to the output of the front-end electronics and the data acquisition system. The

results should resemble closely the real data that will be produced by the detector.

- **Fast simulation:** The detector response is simulated via appropriate parameterisations or other techniques that do not require the full particle transport.

The `AliSimulation` class provides a simple user interface to the simulation framework.

Reconstruction

Most of the ALICE detectors are tracking detectors. Each charged particle going through them leaves a number of discrete signals that measure the position of the points in space where it has passed. The task of the reconstruction algorithms is to assign these space points to tracks and to reconstruct their kinematics. This operation is called track finding.

In ALICE it is required a good track-finding efficiency for tracks down to $p_T = 100\ MeV/c$ even at the highest track density, with occupancy of the electronics channels exceeding 40% in the TPC inner rows at the maximum expected track multiplicity. Given this situation, most of the development is done for Pb–Pb central events, since lower multiplicities are considered an easier problem once the high-multiplicity ones can be handled. However, the opposite may be true for some quantities, such as the main vertex position, where a high track multiplicity will help to reduce the statistical error.

The following terms usually describes data at different step of reconstruction, showed on the right part of *Figure 3.9* and highlighted in *Figure 3.11*:

- *RAWS*: This is a digitized signal (ADC count) obtained by a sensitive pad of a detector at a certain time.

- *RECS*: Reconstructed space point. This is the estimation of the position where a particle crossed the sensitive element of a detector (often, this is done by calculating the center of gravity of the 'cluster').

- *ESD*: Reconstructed track. This is a set of five parameters (such as the curvature and the angles with respect to the coordinate axes) of the particle's

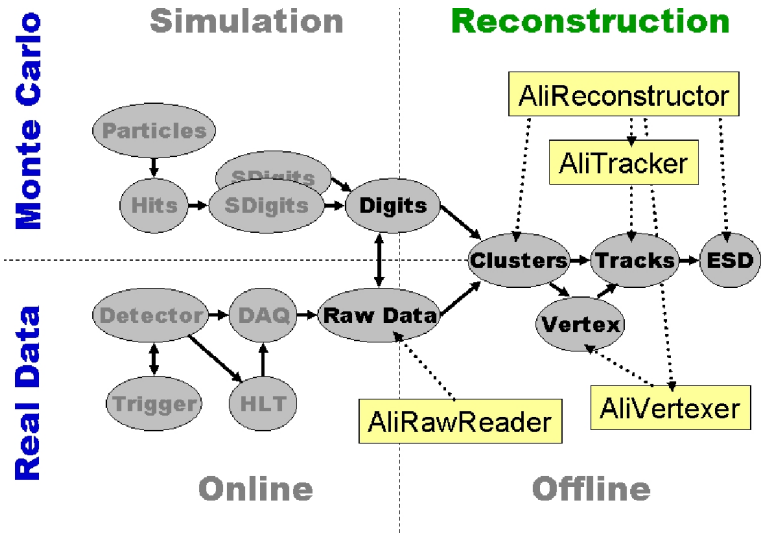

Figure 3.11: *Reconstruction framework.*

trajectory together with the corresponding covariance matrix estimated at a given point in space.

The input to the reconstruction framework are digits in ROOT `TTree` format or Raw Data format. First a local reconstruction of clusters is performed in each detector. Then vertices and tracks are reconstructed and particle types are identified. The output of the reconstruction is the Event Summary Data (ESD). The `AliReconstruction` class provides a simple user interface to the reconstruction framework.

Fast Simulation

The high luminosity and the center of mass energy of LHC make it a high statistics "particle factory". The expected number of quarkonium (charmonium in particular) states detected in the muon spectrometer could be hardly produced and analyzed by full simulations in a reasonable amount of time. So a new kind of approach was adopted in heavy quarkonia production: the fast simulation.

This technique is based on the parametrization of the response of the muon spectrometer at the single muon level, which allows to considerably reduce the requested computational time.

Given a muon of momentum p, genearted at the interaction point at angles θ and ϕ,

the fast simulation applies the smearing of the apparatus and gives the recunstructed p', θ' and ϕ', together with the detection probability P_{det} for that muon. This last term is the product of three fators, giving the probability for that muon to satisfy the acceptance (P_{acc}), reconstruction (P_{rec}) and trigger (P_{trig}) requirements.

The first step toward the fast simulation is the so-called "fast reconstruction" of the muon track in the tracking system of the muon spectrometer. This procedure allows to skip the time consuming digitization and clusterization processes. Starting from a sample of muons coming from full simulations, the residual distributions are created and then parametrized by a superposition of two gaussians and a constant. The residual is defined as $\Delta y = y_{cluster} - y_{hit}$, where $y_{cluster}$ is the impact point coordinate obtained with the cluster reconstruction, while the y_{hit} is the generated hit coordinate.
Parametrizations obtained can be applied to reconstruct the Υ and J/ψ invariant mass spectra with the proper p_T cut. The process still needs the creation of hits, but the skipping of digitization and clusterization leads to a considerable speed gain.

The second step consists in the elimination of the hits creation phase. The objective is actually to direct smear the kinematic variables for each single muon, passing from generation to detector response without any intermediation. In order to obtain this result it is first necessary to parametrize the experimental resolution on the kinematical variables of the muons ($\Delta p = p_{rec} - p_{gen}$, $\Delta\theta = \theta_{rec} - \theta_{gen}$, $\Delta\phi = \phi_{rec} - \phi_{gen}$), together with the acceptance and efficiency in several (p,θ,ϕ) intervals. To this end 3-D grids have been prepared (*Look Up Tables*) in which parameters for the acceptance and for the reconstruction and trigger efficiencies are stored.

Comparison with full simulation shows a very good agreement in the region of $p > 8GeV$, but some discrepancies are present at very low momenta. The phase space portion with $p < 8GeV$ is quite peculiar, showing steep variations due to the fast rise of acceptance and efficiency. In any case the accepted muons is about the same for full and fast simulation, even in the problematic region.

Chapter 4

Υ polarization with ALICE Dimuon Spectrometer

A feasibility study of the Υ polarization measurement in the ALICE dimuon spectrometer has been performed both for p-p collisions and for Pb-Pb collisions.
For p-p collisions the background contribution has been neglected and a 3-D Acceptance matrix method has been used, while background subtraction has been investigated for Pb-Pb collisions and a Monte-Carlo templates method has been applied.
The reference frames considered for the analysis are Helicity and Collins-Soper (see *Section 2.1.1*).
The study of the polarization has been brought back to the study of the angular distribution of the muons produced by the decay of the bottomonium (see *Chapter 2*) and so the reconstruction of the α parameter is related to the fit of a $cos\theta$ spectrum (where with θ, from here on, we address to the polarization angle).
All simulations and reconstructions have been made using the AliRoot framework and Geant3 (see *Section 3.4*).

4.1 3-D Acceptance Matrix Method (AMM)

In order to compare a reconstructed $cos\theta$ distribution to the quadratic trend in *Equation 2.2* the problem of geometrical acceptances and efficiencies of the ALICE apparatus has to be taken into account. The acceptance (from now onwards with this name we refer to both geometrical acceptance and efficiency) is defined as the ratio

between the number of events reconstructed and the number of events generated for each point of the phase-space. If for instance we decide to measure the p_T of muons collected in the ALICE dimuon spectrometer, we would obtain a p_T spectrum that is not comparable to the predicted spectrum for a particular physical process: in order to obtain something comparable, every recontructed point of the phase-space has to be multiplied bin-by-bin by a number that takes into account that some events haven't been collected because of the fact that the detector is not ideal and it doesn't provide a full space coverage. When many kinematical variables are involved, the possible correlations between the acceptances have to be taken into account; in this case two methods can be used:

- a 1-dimensional method in which unidimensional acceptance corrections are obtained with an iterative procedure in order to tune the input distributions of the kinematical variables;

- a multidimentional method in which an acceptance correction is provided for each n-dimensional vector in the phase-space.

To study quarkonium polarization we are usually interested in the transverse momentum of the resonance, in the rapidity and in the $cos\theta$ spectrum from which we extract the α parameter[1] so a 3-D acceptance matrix method has been chosen.
Acceptance matrices are obtained with a Monte-Carlo generation of a wide number of events with "flat" kinematical variables [2] and a reconstruction which takes into account the geometry and the efficiencies of the detector: by calculating $\frac{\#reconstructed}{\#generated}$ for each bin of the n-dimensional matrix the weight value is provided. To be as accurate as possible it's necessary to have narrow bins in order to be sure that in each bin the 3D acceptance surface can be locally approximated with a flat distributon. For this reason a very large number of generated events has to be provided in order to have several reconstructed events for each bin. For our study 10^7 $\Upsilon(1S)$ have been

[1] Acceptances on these three kinematical variables are correlated. If, for example, the $cos\theta$ of the μ^+ is near to 1 in the Helicity reference frame, then the μ^- (produced back-to-back in the Υ C.M. frame) is produced in the opposite direction with respect to the Υ momentum and the p_T of the μ^- will be very low: it is very probable that the μ^- will not pass the trigger, so the acceptance on p_T influences the acceptance on $cos\theta$

[2] This is done to have the same number of generated events for each bin of the acceptance matrix

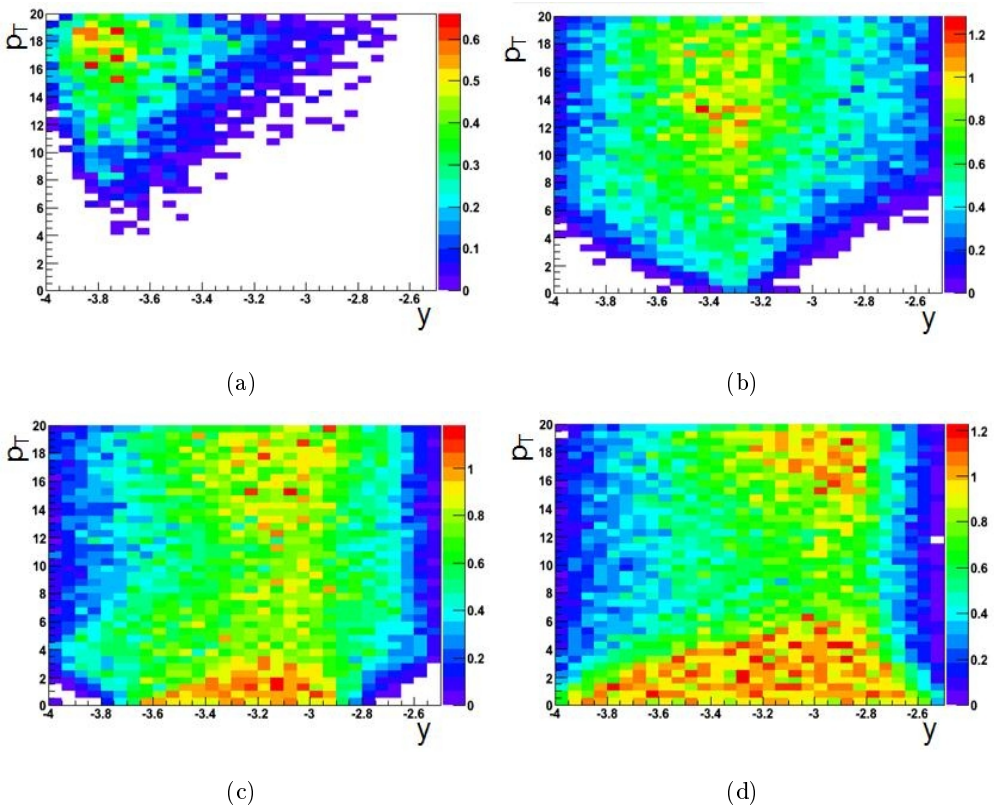

Figure 4.1: Acceptance matrix projections in four $cos\theta$ bins (4.1(a): $-1 < cos\theta < -0.9$; 4.1(b): $-0.7 < cos\theta < -0.6$; 4.1(c): $-0.4 < cos\theta < -0.3$; 4.1(d): $-0.1 < cos\theta < 0$) for $\Upsilon(1S)$ and Helicity polarization angle

generated with flat p_T, y and $cos\theta$ distributions in the ranges:

$$0 \text{ GeV } < p_T < 20 \text{ GeV} \qquad -4 < y < -2,5 \qquad -1 < cos\theta < 1,$$

considering 20 p_T bins, 15 y bins and 20 $cos\theta$ bins.
In *Figure 4.1* four of the 20 acceptance matrices in y and p_T in four particular $cos\theta$ bins are shown.

Once tha acceptance matrix has been prepared, a fiducial region in which the study of the polarization can be performed has to be chosen to avoid acceptance corrections ranging on too many orders of magnitude. For this purpose an "overview matrix" has been generated: a $cos\theta$ range is chosen and for this range every bin of the acceptance matix is checked in order to find if the acceptance value exceeds a

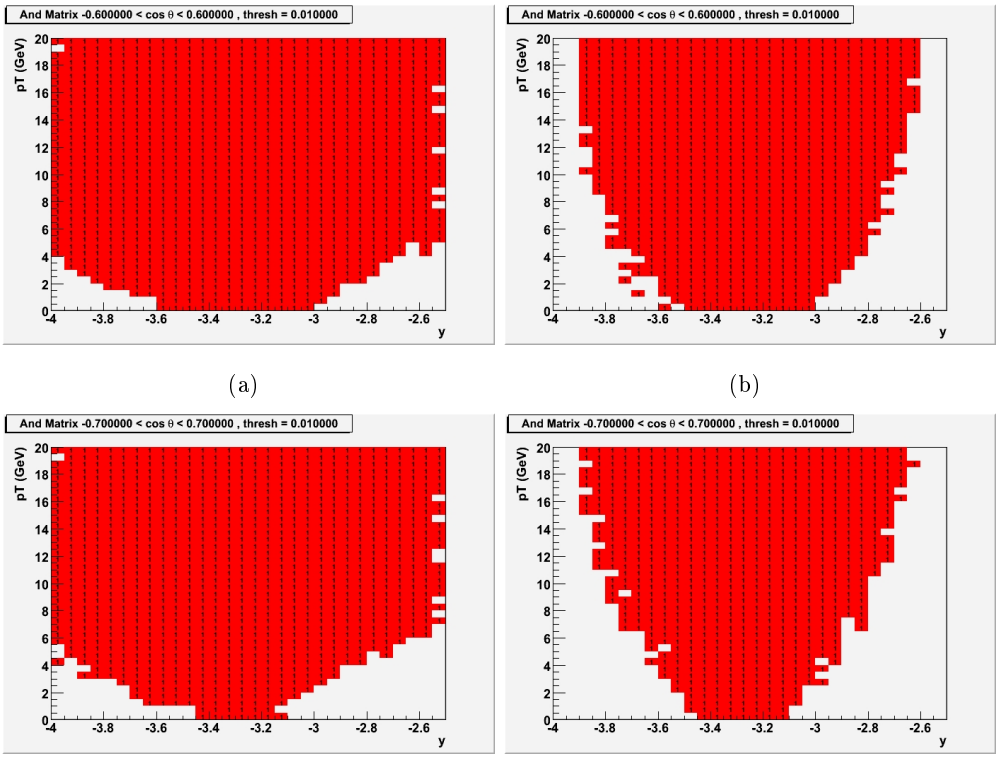

Figure 4.2: Overview acceptance matrices for $\Upsilon(1S)$ in Helicity (left side) and Collins-Soper (right side) angles: two $cos\theta$ ranges corresponding to $-0,6 < cos\theta < 0,6$ (4.2(a) and 4.2(b)) and $-0,7 < cos\theta < 0,7$ (4.2(c) and 4.2(d))

threshold (for us 1%); in this case the bin (i,j) is filled. In all the filled bins the study can be done without having excessive oscillations in the acceptance values (in the worst case 2 orders of magnitude). Four exemples (two for the Helicity angle and two for the Collins-Soper angle) of this overview matrices for the ranges $-0,6 < cos\theta < 0,6$ and $-0,7 < cos\theta < 0,7$ can be found in *Figure 4.2*.

The binning of the acceptance matrix has to be chosen in order to accurately correct reconstructed data: this check has been done generating realistic distributions of the kinematical variables (for $cos\theta$ a transverse polarization has been imposed), correcting the reconstructed data with the acceptance values and then projecting the results on the kinematical variable under study (integrating over the other kinematical variables). The result of such a test for each kinematical variable is shown in

Figure 4.3: the reconstruction is very accurate so the binning chosen is suitable and the method can be used for the analysis.

4.2 Study in p-p collisions

Considering the high value of the S/B ratio (see *Table 4.5*) the study of the α parameter reconstruction for the $\Upsilon(1S)$ for proton-proton collisions has been done negleting the background contribution and using the described AMM. The work can be divided in two parts:

1. reconstruction of the α parameter integrating over the other kinematical variables (global α reconstruction);
2. study of the α reconstruction capability in p_T bins.

4.2.1 Preparing data samples

The $\Upsilon(1S)$ event generation has been done using AliGenParam with the default parametrization (corresponding to to p-p collisions) and the reconstruction has been performed using the full-simulation approach. Two data samples of 10^5 events have been prepared, one with transverse polarization and the other with longitudinal polarization: using this two data samples every degree of polarization can be obtained by the mixing of the two, following the *Equation 2.1*.

4.2.2 Global α reconstruction

This analysis has been done considering 1 year of data taking statistics at nominal luminosity (27100 $\Upsilon(1S)$ in $t = 10^7 s$ at $L = 3 \cdot 10^{30} cm^{-2} s^{-1}$) and three different degrees of polarization (1, 0, -1). The range of variability for the kinematical variables taken into account is:

$$0 \text{ GeV} < p_T < 20 \text{ GeV} \quad -3.6 < y < -3 \quad -0.6 < cos\theta < 0.6$$

both for the helicity angle an the Collins-Soper angle. This range has been chosen with the "overview matrix" method, in fact this fiducial region is (almost) completely covered by acceptances bigger than 1% (see *Figure 4.2*).
After the kinematical cuts about 13000 Υ have been corrected with the acceptance

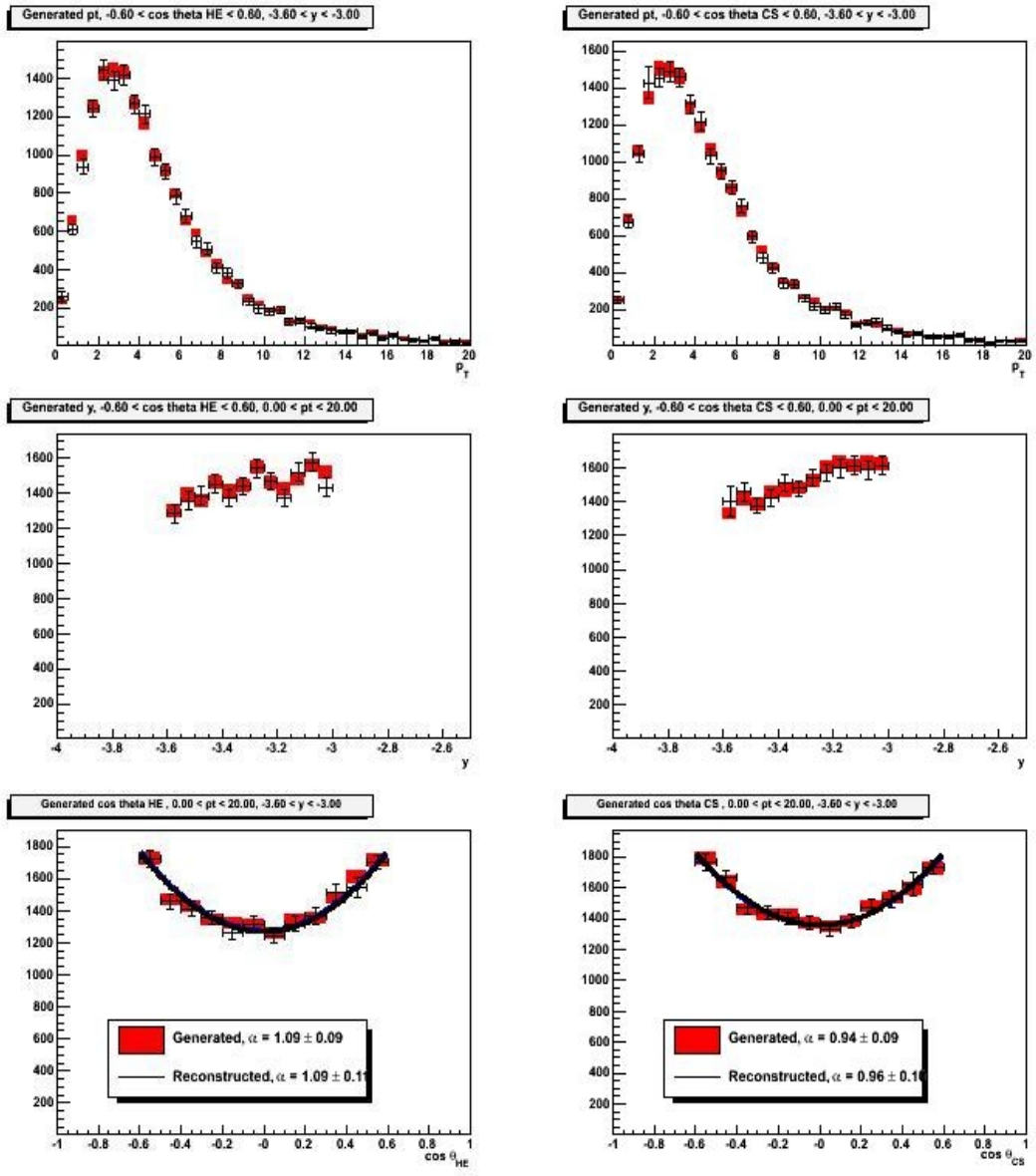

Figure 4.3: Test of the acceptance matrix binning for $\Upsilon(1S)$ transversely polarized in Helicity angle (left side) and in Collins-Soper angle (right side)

$p_T bin(GeV)$	α_{gen}	$\alpha_{rec}(HE)$	$\alpha_{rec}(CS)$
$0 < p_T < 20$	1	1.09 ± 0.11	0.96 ± 0.10
	0	0.02 ± 0.09	0.02 ± 0.08
	-1	-1.04 ± 0.05	-0.94 ± 0.05

Table 4.1: Reconstructed polarization factor for three different genereted degrees of polarization for each polarization angle (Helicity/Collins-Soper)

values for each $cos\theta$ bin and the resulting $cos\theta$ spectrum has been fitted with a quadratic function: the fits are plotted in *Figure 4.4*, while an overview of the results can be found in *Table 4.1*.

We can see that with the no background approximation the global polarization parameter reconstruction can be done in 1 year of data taking with a statistical error between 0.05 and 0.11 in the helicity reference frame and between 0.05 and 0.10 in the Collins-Soper reference frame.

The error on the α parameter enhances when the polarization gets more transverse: this is a consequence of how the fit is done. In fact in the Least Squares method, when the fitting function is:

$$f(x) = p_0 \cdot (1 + \alpha x^2)$$

for p_0 big with respect to α the error on α is proportional to the inverse of p_0 (see *Appendix B*). As can be seen *Figure 4.5* in our case p_0 (the normalization parameter of the parabola) is bigger in the case of longitudinal polarization (statistics being the same) and so in this case the error is smaller.

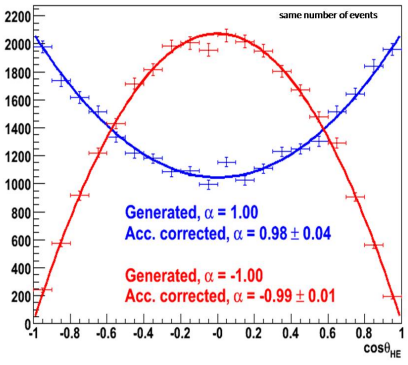

Figure 4.5: Different errors for $\alpha = 1$ and $\alpha = -1$: comparison between the two normalizations

4.2.3 Study of α in p_T bins

For this analysis the same statistics of the previous case has been considered and four p_T bins have been taken into account (the same bins proposed by CDF [11]:

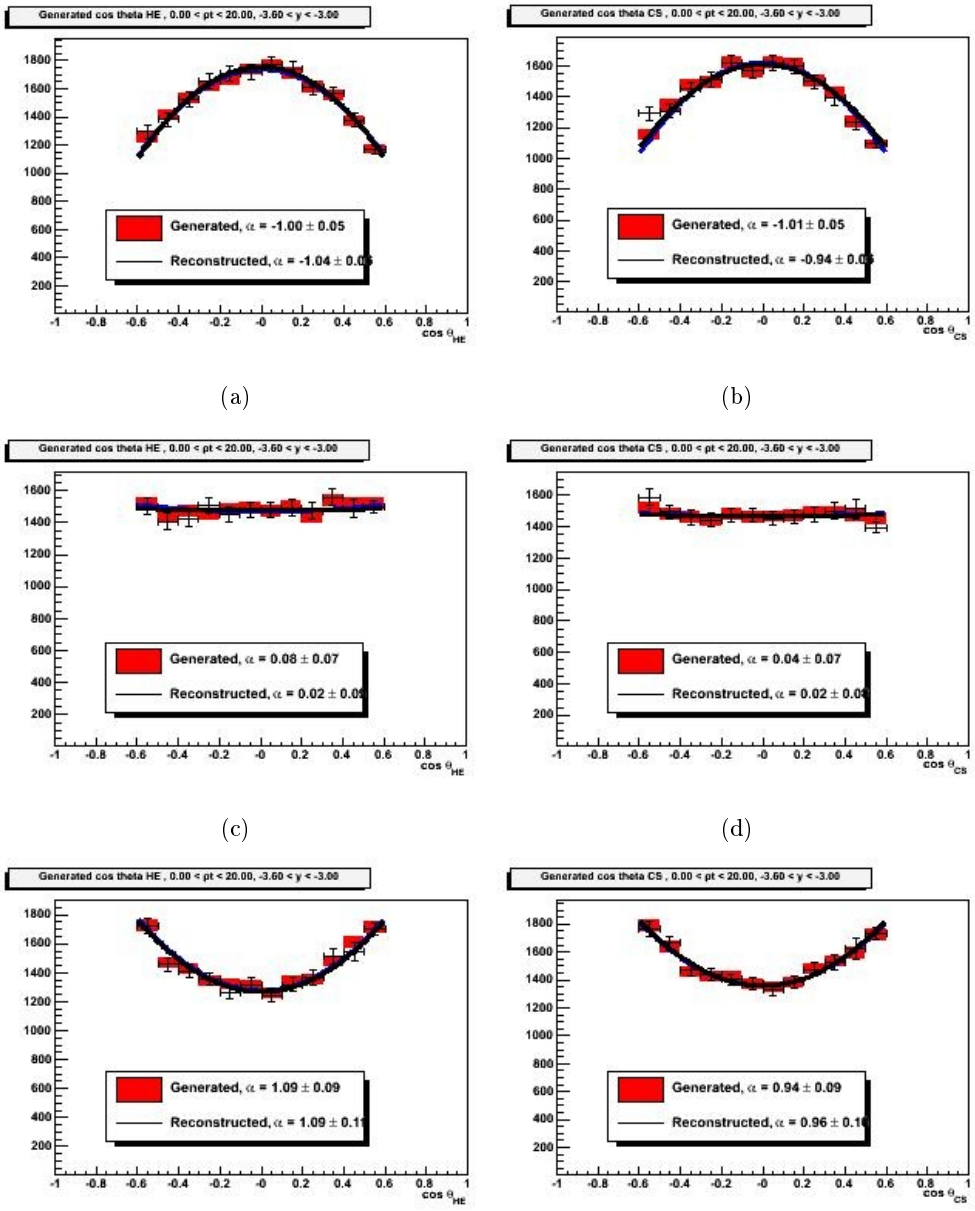

Figure 4.4: Global α reconstruction and correction for acceptances: results of the fits to Helicity spectra (left side) and Collins-Soper spectra (right side)

	p_T	0-3 GeV	3-5 GeV	5-8 GeV	8-20 GeV
HE	y	$-3.6 \div -3$	$-3.9 \div -2.9$	$-4 \div -2.7$	$-4 \div -2.85$
	$cos\theta$	$-0,6 \div 0,6$	$-0,7 \div 0,7$	$-0,7 \div 0,7$	$-0,9 \div 0,9$
CS	y	$-3.6 \div -3$	$-3.6 \div -2.9$	$-3.65 \div -2,9$	$-3.6 \div -2,9$
	$cos\theta$	$-0,6 \div 0,6$	$-0,6 \div 0,6$	$-0,7 \div 0,7$	$-0,8 \div 0,8$

Table 4.2: Variability ranges for $cos\theta$ and y for each p_T bin

0-3 GeV, 3-5 GeV, 5-8 GeV and 8-20 GeV). What can be changed in this case is the range of the kinematical variables: for each p_T bin, in fact, a different window can be chosen to maximize statistics. With the method described in the previous section (using the overview acceptance matrices) a study of the most advisable ranges has been done and the results can be found in *Table 4.2*.

In the ranges specified, the α parameter has been reconstructed and corrected for the acceptances for each p_T bin. Results are summarized in *Table 4.3* and plotted in *Figure 4.6* and we can stress that in this case the difference between α_{gen} and α_{rec} is almost at all times consistent with zero.

In *Table 4.3* the number of reconstructed Υ for each p_T bin are shown: the value remains almost constant and this tells that this choice of the p_T bins will allow to have comparable errors between the bins.

It is interesting to compare statistics obtained at CDF Run Ib in 3 years of data taking (1993-1995) with what we expect in ALICE in 1 year of data taking (see *Table 4.4*):

- for the $\Upsilon(1S)$ statistics will be 3 times higher in ALICE than in CDF, so that smaller errors could be achievable or a finer p_T binning could be considered;
- for the $\Upsilon(2S)$ a study like the one done for $\Upsilon(1S)$ at CDF could be performed;
- for the $\Upsilon(3S)$ maybe only an integrated-p_T study could be done in 1 year of data taking.

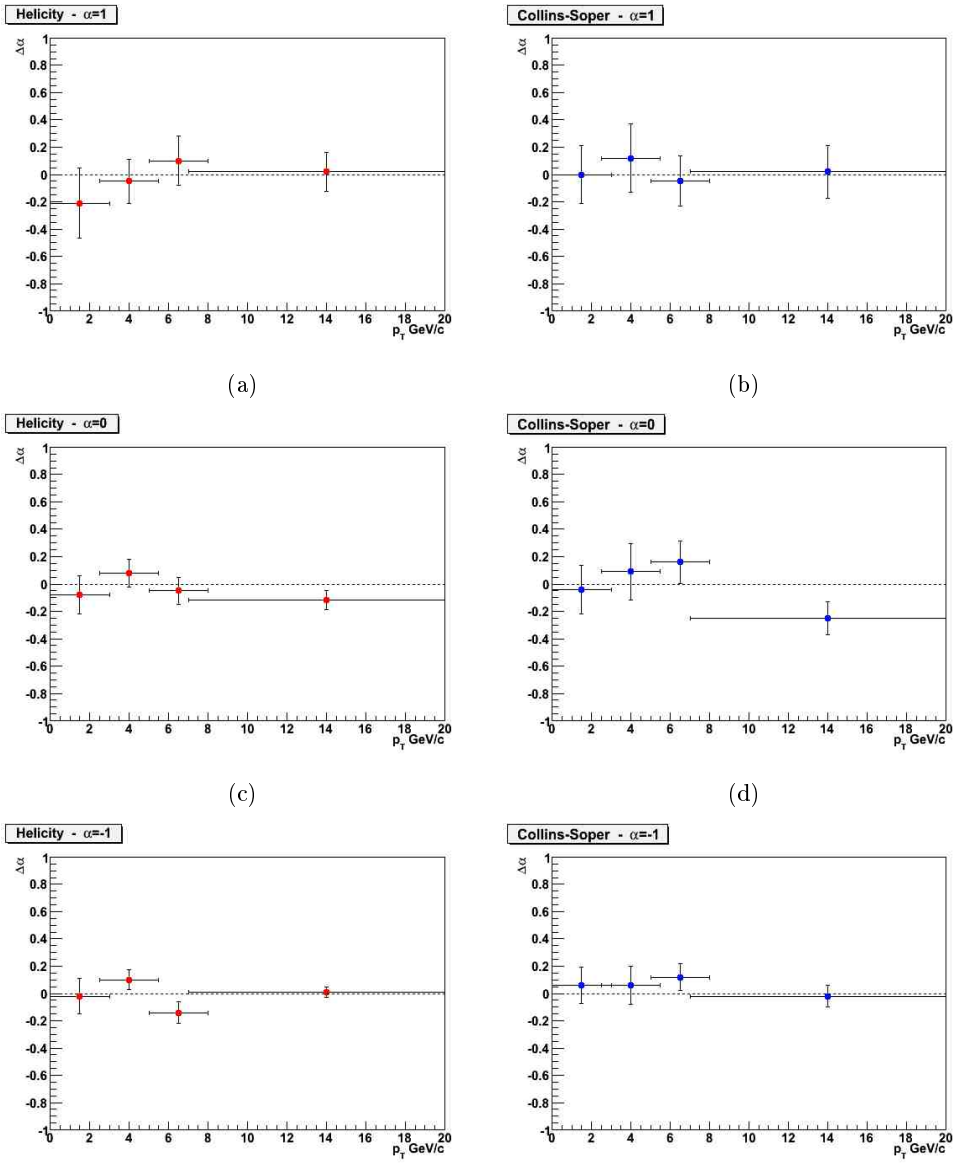

(a) (b)

(c) (d)

(e) (f)

Figure 4.6: Difference between the reconstructed and the generated polarization parameter in four p_T bins: Helicity (4.6(a), 4.6(c) and 4.6(e)) and Collins-Soper (4.6(b), 4.6(d) and 4.6(f)) angles

p_T bin (GeV)	α_{gen}	$\Delta\alpha(HE)$	$\Delta\alpha(CS)$	$\#\Upsilon_{rec}(HE)$	$\#\Upsilon_{rec}(CS)$
$0 < p_T < 3$	1	-0.21 ± 0.25	0.00 ± 0.21	~ 5100	~ 4900
	0	-0.11 ± 0.18	-0.04 ± 0.18		
	-1	-0.02 ± 0.13	0.06 ± 0.13		
$3 < p_T < 5$	1	-0.05 ± 0.16	0.12 ± 0.25	~ 5600	~ 4700
	0	0.14 ± 0.12	0.09 ± 0.21		
	-1	0.10 ± 0.07	0.06 ± 0.14		
$5 < p_T < 8$	1	0.1 ± 0.18	-0.05 ± 0.18	~ 5100	~ 4600
	0	-0.04 ± 0.12	0.16 ± 0.16		
	-1	-0.14 ± 0.08	0.12 ± 0.10		
$8 < p_T < 20$	1	0.02 ± 0.14	0.02 ± 0.19	~ 4000	~ 3500
	0	-0.02 ± 0.09	-0.25 ± 0.12		
	-1	0.01 ± 0.04	-0.02 ± 0.08		

Table 4.3: Difference between the reconstructed and the generated polarization parameter in four p_T bins for the Helicity and the Collins-Soper angles

	Υ_{rec} after kin. cuts	
	CDF	ALICE
$\Upsilon(1S)$	$\sim$4400	$\sim$13000
$\Upsilon(2S)$	$\sim$1100	$\sim$3400
$\Upsilon(3S)$	$\sim$580	$\sim$2000

Table 4.4: Comparison between statistics for p-p in CDF (Run I) and in 1 year of data taking at ALICE (nominal luminosity)

	S/B					
	p-p coll.	Pb-Pb coll.				
		c1	c2	c3	c4	c5
$\Upsilon(1S)$	10.4	1.7	2.3	3.6	6.1	9.1
$\Upsilon(2S)$	3.4	0.65	0.92	1.4	2.2	3.5
$\Upsilon(3S)$	2.4	0.48	0.64	0.99	1.6	2.2

Table 4.5: Statistics expected in ALICE for p-p collisions and Pb-Pb collisions for each centrality class

4.3 Background subtraction

As we can see in *Table 4.5* the background contribution is small in proton-proton collision, but not completely negligible, so that the results obtained with the described procedure could be too optimistic: the presence of a background contribution under the resonance peak could introduce a bias in the determination of the α parameter if not subtracted.

It's straightforward that in case of lead-lead collisions things go worse than in the first case: if we consider the S/B ratio in the five centrality classes (see *Table 4.5*) we conclude that for small values of the impact parameter the ratio is really small and so the bias introduced by not subtracting the background contribution would become very big. So it's clear that to study the Υ polarization (surely for Pb-Pb collision, but maybe also for p-p collisions) the problem of the background subtraction plays an important role.
To cope with this problem the procedure used to reconstruct α has to be changed because the 3-D acceptance matrix method is not advisible in this case: in principle the background should be subtracted cell by cell in the acceptance matrix, but this would be accurately feasible (because of the large number of cells) only with an extremely high statistics signal. It is therefore necessary to use an alternative way to estimate the polarization parameter without the use of an acceptance matrix: the method chosen for the analysis is the Monte-Carlo Templates method, proposed and used by CDF [11].

4.4 The Monte-Carlo Templates Method (MCTM)

If the data sample is contamined by a sizable background and we are interested in the trend of a specific kinematical variable (e.g. the $cos\theta$ spectrum) we can subtract the background contribution bin-by-bin. The Monte-Carlo Templates method consists of the following passages:

1. the data sample is divided in several $cos\theta$ bins (e.g. 20);

2. for each $cos\theta$ bin a mass spectrum is provided and each mass spectrum is opportunetely fitted;

3. each fit allows the determination of the background yield (B) in a particular mass window (under the resonance peak) by the integration of the background fitting function;

4. in the same mass window data are counted and this gives the Signal+background contribution in each $cos\theta$ bin (S+B);

5. finally all the S+B values are plotted in a $cos\theta$ spectrum and fitted with a linear superposition of two templates (one transversely and one longitudinally polarized) plus the B contributions: the coefficients of the linear superposition give the value of the α parameter:

$$\begin{aligned} F_{S+B}(cos\theta) &= \xi_L \cdot T_L(cos\theta) + \xi_T \cdot T_T(cos\theta) + B(cos\theta) \\ &= \frac{1-\alpha}{3+\alpha} \cdot T_L(cos\theta) + \frac{2(1+\alpha)}{3+\alpha} \cdot T_T(cos\theta) + B(cos\theta) \end{aligned} \quad (4.1)$$

Templates are $cos\theta$ spectra extracted from signal data samples obtained by reconstructing a large number of generated data to which an extreme polarization had been previously imposed (as stated before usually a transversely and a longitudinally polarized samples are considered). It's very important that the two templates are obtained starting from an equal number of generated events to take care in the right way of the acceptances and efficiencies effects.
In our analysis 10^5 logitudinally and 10^5 transversely polarized $\Upsilon(1S)$ generated events have been used to obtain the templates shown in *Figure 4.7*.

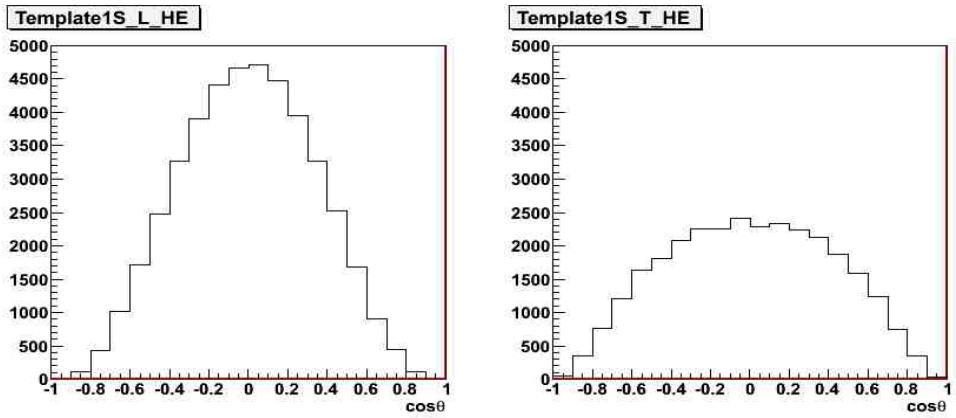

(a) (b)

Figure 4.7: Templates: longitudinal (4.7(a)) and transversal (4.7(b)) shapes for reconstructed $\Upsilon(1S)$ data from the same number of generated events

The fit to the S+B $cos\theta$ spectrum is usually done with the Root MINUIT package and the quantity which has to be minimized is:

$$\chi^2 = \frac{1}{2} \cdot \sum_i (E_i + \beta_i - D_i) - D_i ln\left(\frac{E_i + \beta_i}{D_i}\right) + (\beta_i - S_i) - S_i ln\left(\frac{\beta_i}{S_i}\right) \qquad (4.2)$$

where:

- i runs over all the $cos\theta$ bins;
- D_i is the S+B value;
- S_i is the B value;
- $E_i + \beta_i$ is the expected number of S+B events, where E_i refers to the signal alone and β_i to the background alone. The last one is obtained by the data and by the previous one by imposing that

$$\frac{\partial \chi^2}{\partial \beta_i} = 0$$

and by choosing the only physical solution:

$$\beta_i = \frac{1}{4}\left(-(2E_i - D_i - S_i) + \sqrt{(2E_i - D_i - S_i)^2 + 8S_iE_i}\right)$$

The *Formula 4.2* is the one used in the CDF analysis [11] and is correct only when both the S+B and the B errors are poissonian. In our procedure only the S+B number is obtained by counting events (and so has a Poisson-like error), but the B value is an inegral of a function, which is not poisson-distributed. However it is not trivial to find out an alternative quantity to be minimized which takes into account this caveat and, moreover, the underestimation of the error done considering it poissonian seems to be not so large. So, in the study presented below, the formula proposed by CDF has been used in the approximation of poisson-distributed background contribution.

4.5 Study in Pb-Pb collisions

MCTM being the method to be used, an analysis of the worst case for what concerns background subtraction (Pb-Pb collisions) has been made: if the polarization estimation works in this case it surely could be applied also to the case of proton-proton collisions.

4.5.1 Signal and Background Simulation

The first step of this analysis is the generation of $\mu^+\mu^-$ pairs in the mass region between 8 and 12 GeV; the choice of the low and high-edges of the mass window is due to the fact that all the three resonances mass spectra are contained in this region and, moreover, two side zones in which the background is the only contribution to the data counting can be identified (8-9 GeV and 11-12 GeV) [3].

Three contributions to the total mass spectrum can be pinpointed: signal (from $\Upsilon(1S)$, $\Upsilon(2S)$ and $\Upsilon(3S)$), correlated background and uncorrelated background. The contribution to the background of π and K mesons can be considered negligible (see *Figure 4.8*) in any centrality class.

In this study 5 centrality classes have been used: for each class the upper and the lower values of the impact parameter are shown in *Table 4.2*. The contributions of signal, correlated and uncorrelated background are more or less important while the impact parameter of the collision changes: the relative weights have been taken from

[3] The necessity of having a background-dominated zone comes from the fact that an accurate estimation of the background has to be done (see *Section 4.4*)

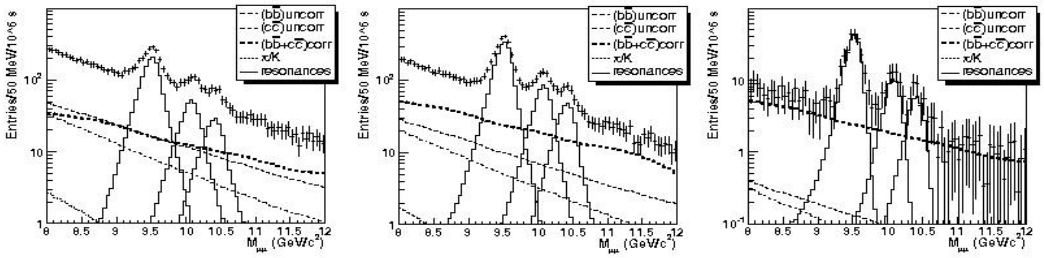

Figure 4.8: Different distributions to the complete mass-spectrum in the 8-12 GeV window [10] for 3 different centrality classes: $0 < b < 3$ (left), $6 < b < 9$ (central) and $b > 12$ (right)

Class Name	c1	c2	c3	c4	c5
b (fm)	0-3	3-6	6-9	9-12	>12
N_{part}	414-375	375-276	276-152	152-54	54-0

Table 4.6: The five centrality classes for Pb-Pb collisions: impact parameters and number of participants

Smbat Grigoryan's work for the PPR Vol.2 [10] (see *Figure 4.8*). The generation of 5 different data samples, one for each centrality class, has been done in order to have the possibility to study the polarization for different impact parameters, but by the time all the work has been made by integrating over all the centrality classes.
Statistics for 1,3 and 5 years of data taking have been considered.

Signal

The generation of $\mu^+\mu^-$ pairs coming from the decay of a ϒ produced in Pb-Pb collisions at 5.5A TeV has been done with the AliRoot full-simulation framework, using a parametrization for the kinematical variables called "Vogt PbPb", which is based on theoretical predictions. Two large samples of ϒ, corresponding to $\alpha = \pm 1$, have been simulated for the three resonances: these two samples are sufficient to generate every kind of polarization with the mixing of the two. In this way several degrees of polarization have been obtained (-1,-0.5,0,0.5,1) and for each of these a data sample has been prepared.

Correlated Background

The correlated part of the background is constituted by two or more unlike-sign muons coming from the same QCD vertex. The main contributions are from $b\overline{b}$ and $c\overline{c}$ which strongly decay as listed below:

$$b\ \overline{b} \longrightarrow \overline{B}^0 + B^+ + X \longrightarrow D^+\mu^-\overline{\nu}_\mu + \overline{D}^0\mu^+\nu_\mu + X \longrightarrow \mu^+\mu^-\overline{\nu}_\mu + \mu^-\mu^+\nu_\mu + X$$

$$b\ \overline{b} \longrightarrow B^- + B^0 + X \longrightarrow D^0\mu^-\overline{\nu}_\mu + D^-\mu^+\nu_\mu + X \longrightarrow \mu^+\mu^-\overline{\nu}_\mu + \mu^-\mu^+\nu_\mu + X$$

$$c\ \overline{c} \longrightarrow D^+ + \overline{D}^0 + X \longrightarrow \mu^+ + \mu^- + X$$

$$c\ \overline{c} \longrightarrow D^0 + D^- + X \longrightarrow \mu^+ + \mu^- + X$$

To the examples listed, the cases of B and D mesons mixings have to be added.
For this study an already existing generation have been used[4]: four muons for the bottom part and two muons for the charm part were obtained with Pythia (for more details see [19]). This muon generation have been reconstructed with the fast-simulation approch (see *Section 3.4.1*) so that a 3D histogram [5] of pseudo-events have been prepared. Randomly extracting from this 3-dimensional surface, all the correlated contributions needed can be obtained for each centrality class and for each year of data taking considered.
In *Figure 4.9(a)* the geneareted and reconstructed $cos\theta$ spectrum for the correlated background contribution is shown.

Uncorrelated Background

The uncorrelated part of the background is constituted by two or more unlike-sign muons coming from different QCD vertices. The main difference from the previous case is that here the muons could come from different flavored quarks (e.g. from b c or from b $\overline{c}$). Of course the contribution of this kind of background is more important when the impact parameter is small because in this case the number of partecipants to the collision is big and so a lot of uncorrelated b and c quarks are produced; when the impact parameter enhances the uncorrelated contribution decreases so also the correlated part can play its role.

[4] Thanks to Rachid Guernane for making his work available
[5] The three dimensions correspond to: mass, p_T and $cos\theta$

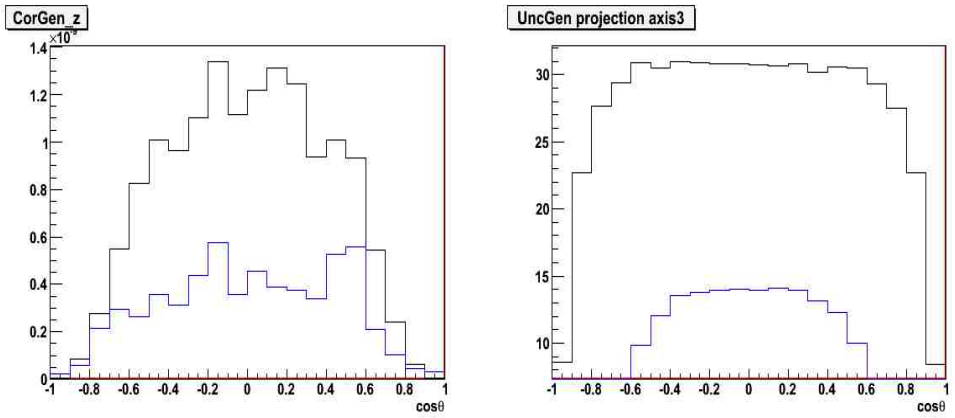

(a) (b)

Figure 4.9: Generated (black line) and reconstructed (blue line) *cosθ* spectra shapes for correlated (4.9(a)) and uncorrelated (4.9(b)) background contributions: bins are filled with weights coming from the fast-simulation

Here the generation has been made by a parametrization of the dimuon kinematical variables (vontained in AliRoot) and the reconstruction through the fast-simulation approach: a 4-dimensional THnSparse (n-dimensional histogram) have been prepared [6] filling it with the weights coming from the fast-simulation so that randomly extracting data from this distribution all the data needed could be obtained.
In *Figure 4.9(b)* the geneareted and reconstructed *cosθ* spectrum for the uncorrelated background contribution is shown.

An example of mass spectrum with all the different contributions can be found in *Figure 4.10* where signal alone (a), signal+corr.bkg (b) and all the data (c) are shown for longitudinally polarized bottomonium states. In *Figure 4.11* the relative contributions of correlated and uncorrelated background are shown in four centrality classes.

4.5.2 Fitting Invariant Mass Spectra

As described in *Section 4.4*, once all the data are in hand, they have to be divided in 20 *cosθ* bins and for each bin a fit to the mass spectrum has to be performed. It is

[6] The four dimensions correspond to: mass, p_T, *cosθ* and y

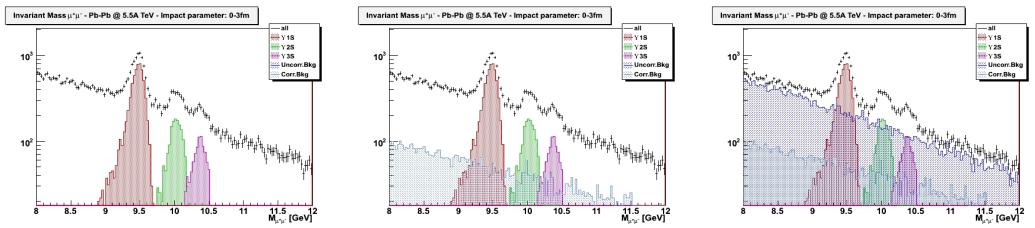

(a) (b) (c)

Figure 4.10: Preparing data sample: signal alone (4.10(a)), signal+corr.bkg (4.10(b)), signal+corr.bkg+uncorr.bkg (4.10(c))

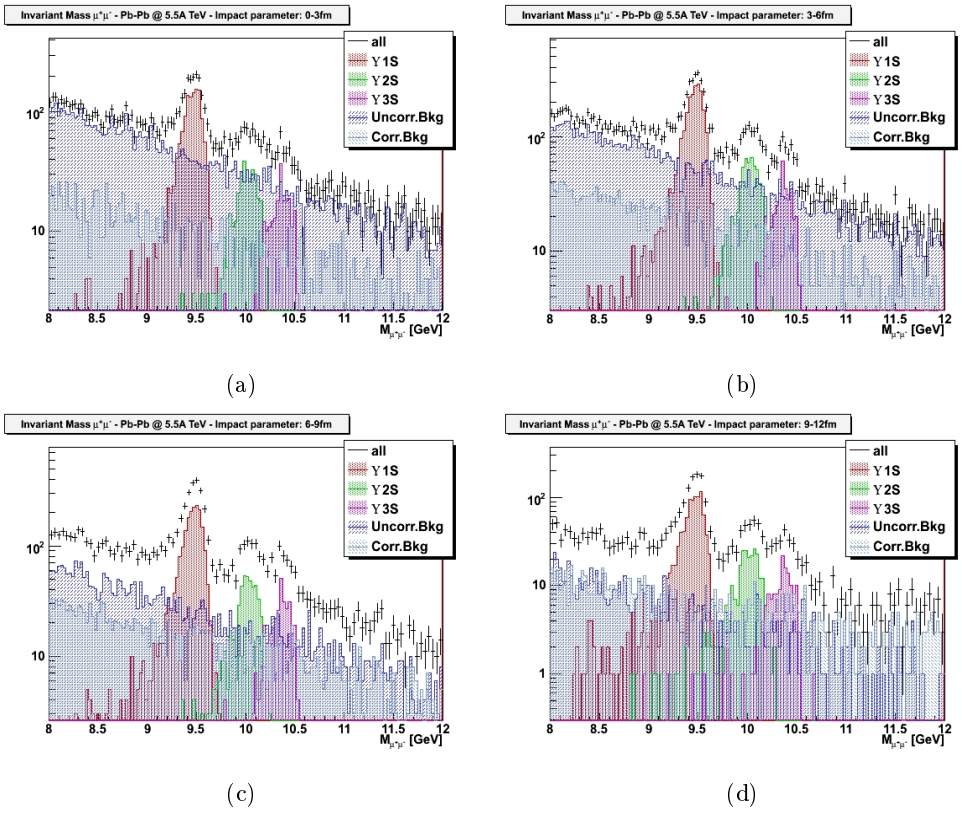

(a) (b)

(c) (d)

Figure 4.11: Relative contributions of correlated and uncorrelated background in four centrality classes for 1 year of data taking

therefore necessary to choose what shape can properly interpolate the data. For this study gaussians with asymmetric tails for the three resonances and an exponential shape for the background heve been used. Of course not all the parameters can be let free because in this case a 35-parameters fit should be performed and the convergence could be very difficult. It is therefore necessary to fix some parameters which have to be estimated with a previous fit to the signal alone: in this way all the parameters can be extrapolated and only the normalization of the fitting curve can be let free. The approach is therefore to let as free the three resonance's normalizations and all the background parameters.
This procedure allows to perform a satisfactory fit for 18 $cos\theta$ bins (the first and the last have nothing much statistics); in *Figure 4.12* all the fits for 1 year of data taking and longitudinal resonances polarization can be found.

The fit has to estimate in the best way the background contribution because is from the integration of the background fitting-function that the background contribution to the $cos\theta$ spectrum is extrapolated.
The 9.2-9.7 GeV mass-window has been chosen for the integration and for the counting of S+B data.
In *Figure 4.13* the fit to the 10th ($-0,1 < cos\theta < 0$) and to the 5th ($-0,6 < cos\theta < -0.5$) mass spectra for a longitudinally polarized sample is shown for 1, 3 and 5 years of data taking. The fits, as stated before, allow to plot a S+B and a B $cos\theta$ spectrum for each degree of polarization: in *Figure 4.14* the case of a 3-year of data taking sample with a $\alpha = 0$ polarization is shown.

Overlaps of the $\Upsilon(1S)$ and $\Upsilon(2S)$ resonances have been considered: to study the $\Upsilon(1S)$ polarization the $\Upsilon(2S)$ contribution has to be considered as background. To take this into account the integral of the $\Upsilon(2S)$ fitting function between 9.2 and 9.7 GeV has been added to the background contribution (B value).

4.5.3 Fitting $cos\theta$ Spectra with Monte-Carlo Templates

The fitting method described in *Section 4.4* allows the determination of the α parameter weighting with the correct ratio transverse and a longitudinally-shaped templates. The results of all the fits done is shown in *Figure 4.15*, where black crosses are the S+B contribution, blue crosses are the B contribution and red dots show the result of the fit. As already underlined before, background errors have been consid-

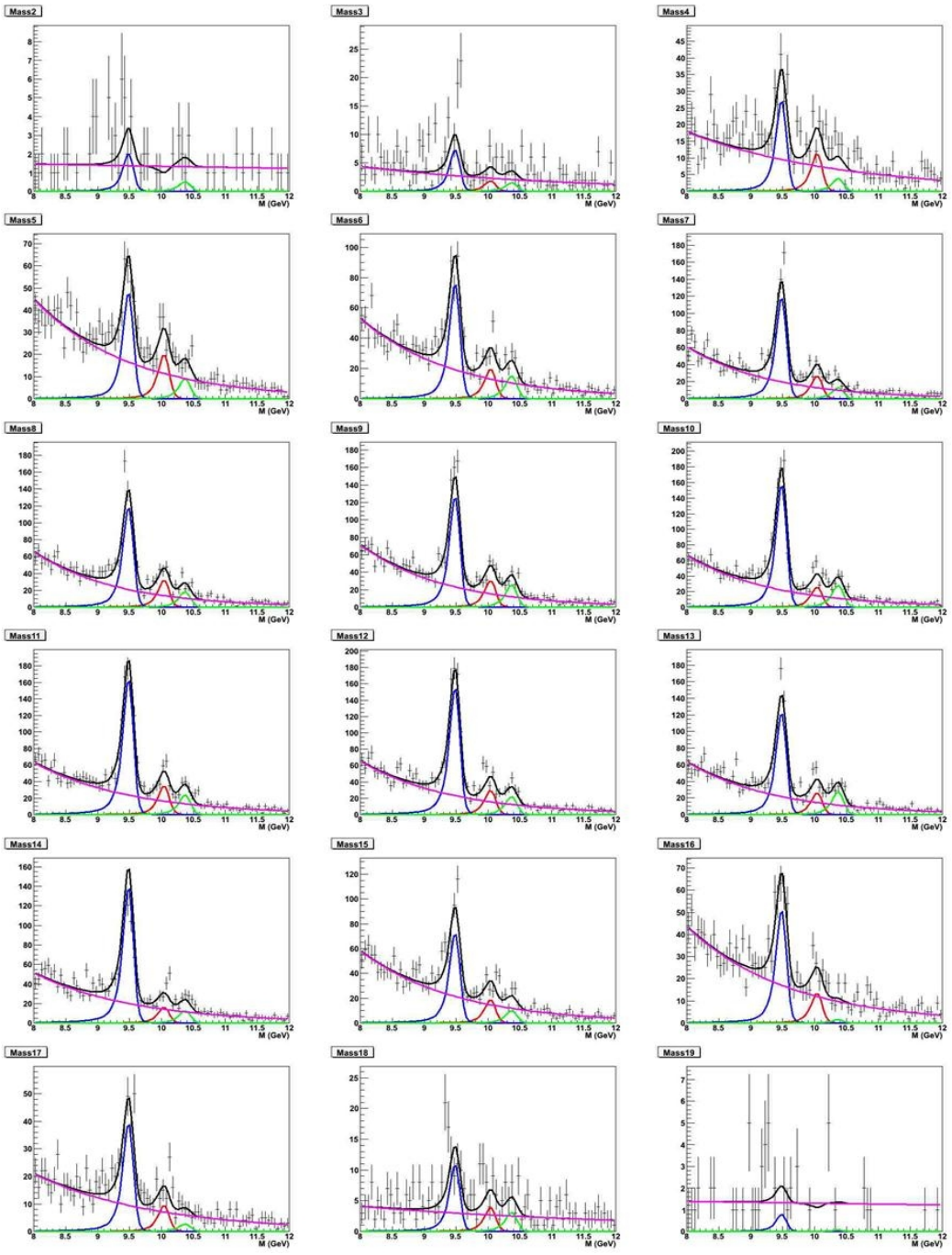

Figure 4.12: Fitted mass spectra: one fit for each $cos\theta$ bin (from -0,9 to 0,9) for a $\Upsilon(1S)$ longitudinally polarized in 1 year of data taking; the black line is the overall fit, in magenta the background fit, in blue, red and green the three resonances fits.

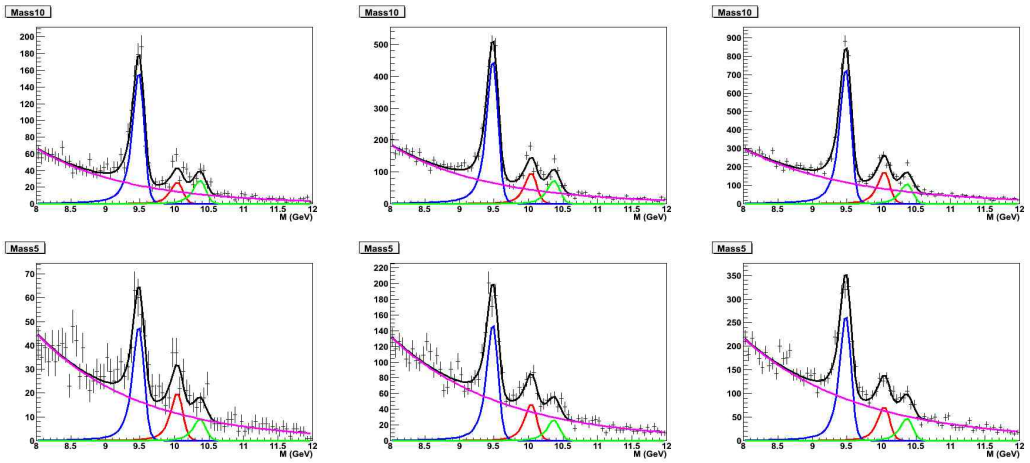

(d) (e) (f)

Figure 4.13: Fitting mass spectra for a longitudinally polarized $\Upsilon(1S)$ sample in 1 (4.13(d)), 3 (4.13(e)) and 5 (4.13(f)) years of data taking: 10th and 5th $cos\theta$ bins (corresponding to $-0,1 < cos\theta < 0$ and $-0,6 < cos\theta < 0,5$)

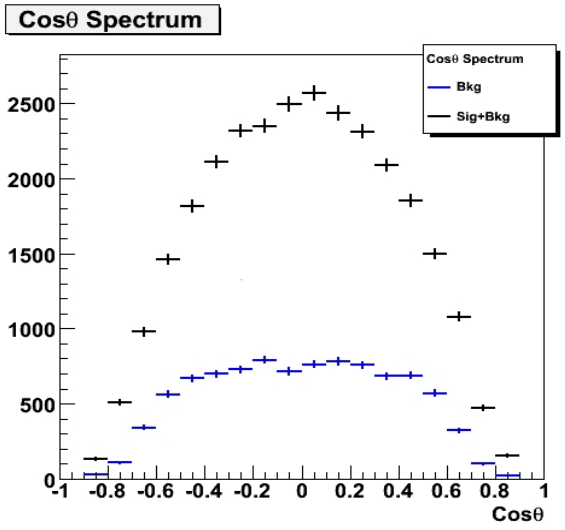

Figure 4.14: $Cos\theta_{HE}$ spectra for S+B and B alone for $\Upsilon(1S)$ with $\alpha = 0$ in 3 years of data taking

ered poissonian while in principle they are not: so a possible underestimation of the error on α could have been done.

An overview of all the results can be found in *Figure 4.16*; looking at this plot some comments can be done:

1. the method allows a general good estimation of the α parameter. Errors are between 0.06 and 0.15 for 1-year statistics, between 0,03 and 0,09 for 3-years statistics and between 0.03 and 0.06 for 5-years statistics;

2. the statistics being the same, there is an increase of the error on α when the polarization becomes more transverse. This effect is analogous to what discussed in *Section 4.2.2* for the proton-proton collisions case: the transversal case has a smaller normalization parameter and so the error is bigger;

3. for high values of α (and particulary for low statistics) there is a little bias in the determination of the polarization parameter; the reason of such an overestimation is discussed in *Section 4.5.4*.

4.5.4 Background shape and α overestimation

As already mentioned in the previous section, for high values of α_{gen} the reconstruction of the polarization parameter is contamined by a bias which leads to sensibly higher values of α_{rec}. This is an effect which happens when the $cos\theta$ spectrum of the signal alone is wider than the transverse template spectrum: in this case the coefficient ξ_T in *Equation4.1* is more than one.
This means that in the edges of the spectrum there is an overestimation of the signal contribution, which in other words means that an underestimation of the background contribution is present. An analysis of the case of an $\alpha = +1$ sample (see *Figure 4.17*) for one year of data taking shows as a matter of fact that this is the exact case:

- *Figure (a)*: in central $cos\theta$ bins the background seems to have a perfect exponential shape and so our integral of the fitting function well estimates the number of background events;

- *Figure (b)*: by the edges of the $cos\theta$ spectrum the background shape changes and a simple exponential fit is not appropriate anymore; the fit stands system-

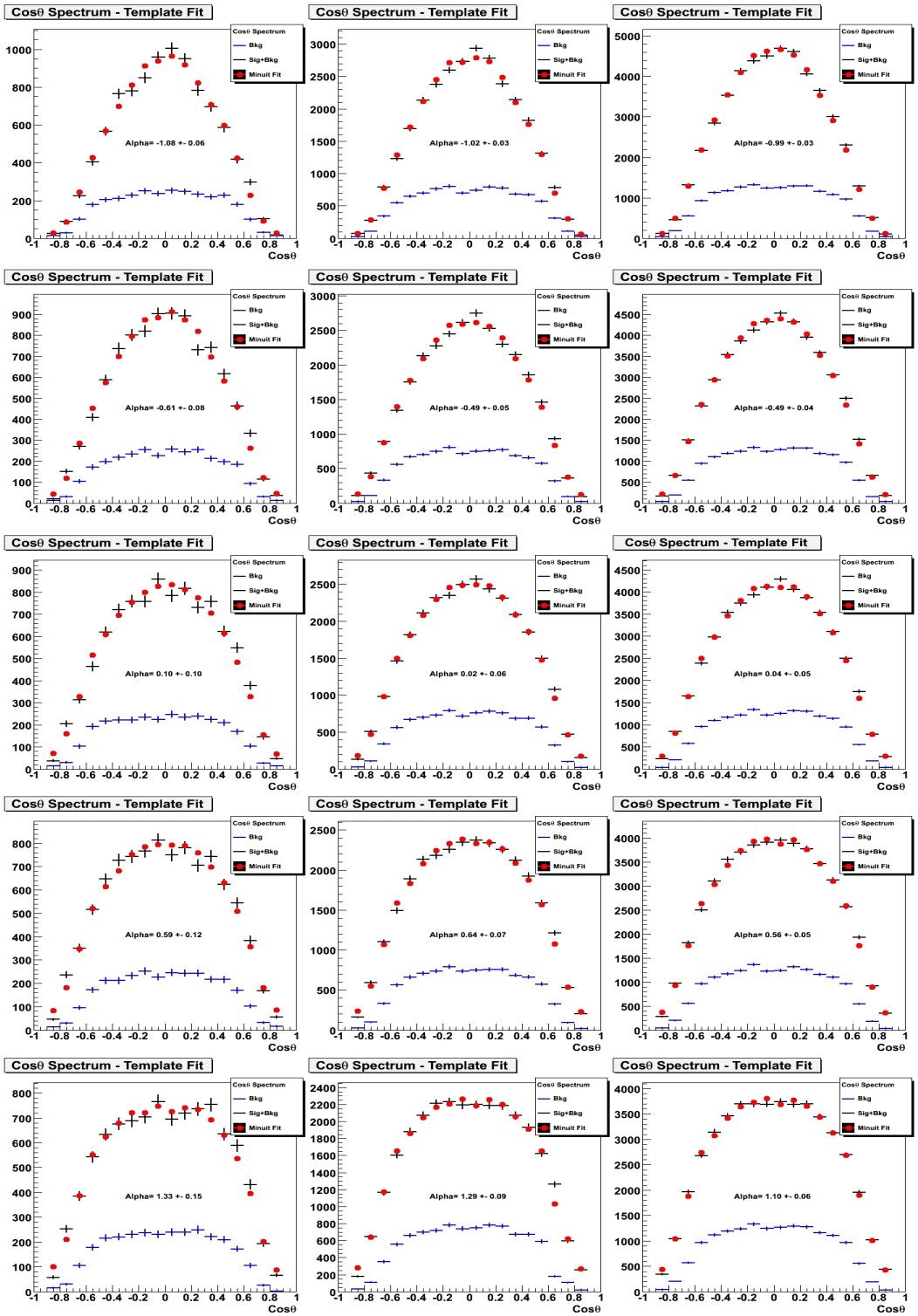

Figure 4.15: Fits to the $cos\theta_H E$ S+B spectra for 1 year (left), 3 years (center), 5 years (right) of data taking. Several polarization (from -1 to 1) are shown in each row

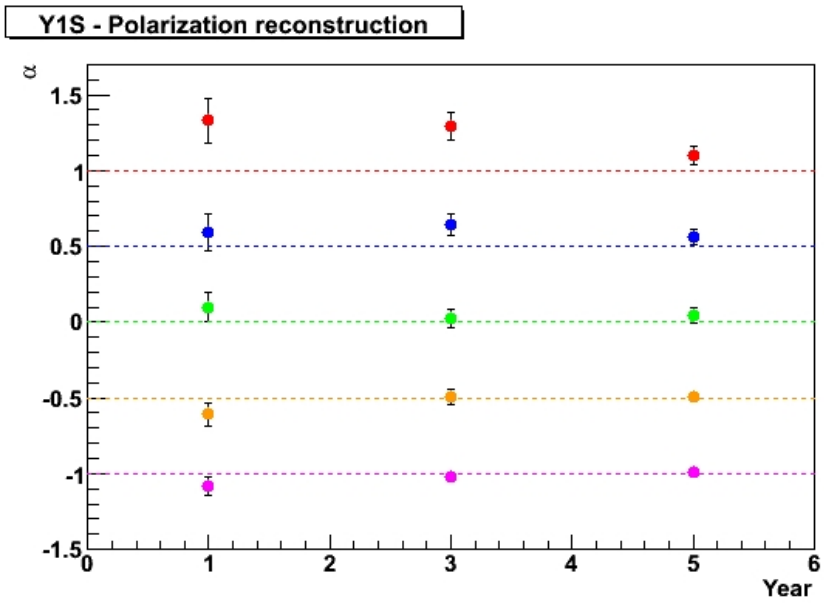

Figure 4.16: Overview of the reconstructed α parameters for $\Upsilon(1S)$ in 1, 3 and 5 years of data taking

atically under the histogram to be fitted in the mass window under study, so an underestimation of the background contribution is made.

The problem is present only when α is near to one because in this case the $cos\theta$ spectrum has a central plateau and it falls down in the regions $-1 < cos\theta < -0.5$ and $0.5 < cos\theta < 1$, so the region in wich the background is underestimated. The plateau doesn't weigh upon the fit, while the falling-down region does. When α is smaller the edges of the $cos\theta$ spectrum are less important because less statistics is present and so in this case the goodness of the fit is hardly dependent on the central part of the spectrum in which the estimation of the fit is satisfactory.

It is not trivial to find an appropriate shape to be used for the fit to the invariant mass spectrum between 8 and 12 GeV: the exponential one grants for all the $cos\theta$ bins the convergence of the fit, while other shapes fit better some regions, but lead to macroscopic mistakes in other cases. Moreover it should be considered that in principle we can not know what is the behaviour of the background under the resonance peak, so only a "sideband extrapolation" can be done.

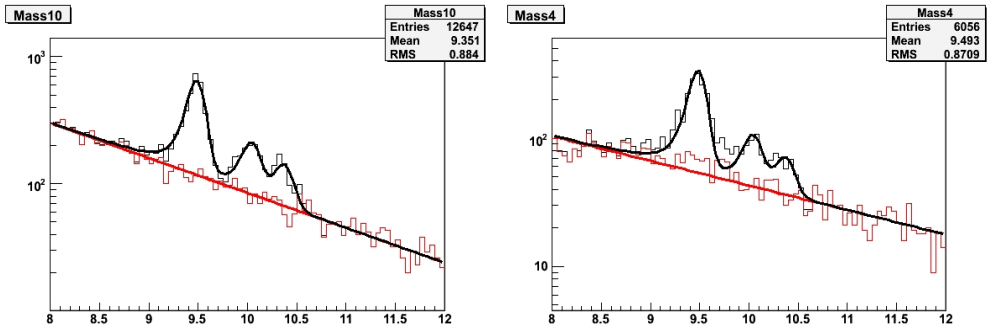

(a) (b)

Figure 4.17: Background fit in two different $cos\theta$ bins for a 1 year of data taking sample of transversely polarized $\Upsilon(1S)$

This effect is so to be considered as a possible bias in case of hardly transverse polarization measurements and, as far as we are confident on our Monte-Carlo simulated background, a study of the bias dependence on the α parameter could be done and the sistematic eliminated.

Chapter 5

Conclusions

An analysis of the Υ polarization in the ALICE dimuon spectrometer has been carried out. The bottomonia resonances can be detected with a mass resolution of $\sim 100 MeV/c^2$. Such a value allows a clear separation of the peaks due to $\Upsilon(1S)$, $\Upsilon(2S)$ and $\Upsilon(3S)$ resonances.
While in proton-proton the signal over background ratio (S/B) is large (about 10 for the Υ), for lead-lead collisions a sizeable background is present (S/B $\sim$ 1.7 for central collisions).

For p-p collisions the background contribution has been neglected in the analysis and a 3-D acceptance matrix method has been used to reconstruct the decay muon distribution and to extract the polarization parameter (α) fitting the data with the expected polar angle distribution $f(\theta) = 1 + \alpha cos^2\theta$. For this method, the choice of the kinematic subranges in y, p_T and $cos\theta$ play a crucial role and has been thoroughly described in the text.

Integrating over all the kinematical variables the polarization parameter for $\Upsilon(1S)$ can be extracted at ALICE in one year of data taking at nominal luminosity ($5 \cdot 10^{30} cm^{-2} s^{-1}$) and the statistical errors on α turn out to be between 0.05 and 0.1.
Thanks to the relatively high statistics ($2.7 \cdot 10^4 \Upsilon / yearinp - p$) a study of the dependence of the α parameter on p_T can be carried out in one year of data taking with statistical errors ranging from 0.03 to 0.19 (using the CDF p_T-binning). This study could be very interesting because it will probe NRQCD in its predictions about

polarization in a rather accurate way.

For Pb-Pb collisions the complete invariant mass spectrum between 8 and 12 GeV has been simulated, taking into account the expected relative ratios between the three resonances and the various background contributions. In this case it's not possible to neglect the background and so a "Monte-Carlo templates method", described in detail in the text, has been used to extract the α parameter.
In one year of data taking at nominal luminosity ($5\dot{1}0^{26} cm^{-2} s^{-1}$) the $\Upsilon(1S)$ polarization can be extracted with an error ~ 0.1; by integrating over some years of data taking a p_T or centrality dependence of polarization can also be investigated.

For what concerns $\Upsilon(2S)$ and $\Upsilon(3S)$ a polarization measurement in p-p might be feasible (integrating over all kinematical variables) in one year of data taking, while in Pb-Pb collisions some years might be necessary.

Appendix A

Υ angular decay distribution

In this Appendix we derive the $(1+\alpha cos^2\theta)$ dependence for the angular distribution of $\mu^+\mu^-$ pairs coming from the decay of a vector meson.
A general discussion on this subject can be found in [25], where also three-body decays are examined.

A.1 The Density Matrix ρ

The decay correlations of an unstable system depend on the total angular momentum j of the system and on the magnetic sub-state populations m for each j.
The information on magnetic sub-state populations is contained in the spin-space density matrix ρ. For a system of angular momentum j at rest the density matrix can be expressed in the (j,m) basis as:

$$\rho = \sum_{mm'} |jm\rangle \rho_{mm'} \langle jm'|.$$

A 1^{--} state has 3 possible values for m an so the density matrix can be written as:

$$\rho = \begin{pmatrix} \rho_{11} & \rho_{10} & \rho_{1-1} \\ \rho_{01} & \rho_{00} & \rho_{0-1} \\ \rho_{-11} & \rho_{-10} & \rho_{-1-1} \end{pmatrix} \tag{A.1}$$

The density matrix is Hermitian and satisfies $Tr(\rho) = 1$; the longitudinal and transverse polarization fractions are ρ_{00} and $(\rho_{11} + \rho_{-1-1})$ respectively[1].

[1] The reason of this can be found remembering that for a spin-1 particle the basis for the spin part

A.2 Derivation

We consider a system Υ with angular momentum j and parity η_Υ which decays into two particles called μ^+ and μ^- with spins s_+ and s_- and intrinsic parities η_+ and η_- respectively.
To obtain an appropriate coordinate system for analyzing the decay the relevant independent vectors are the proton momentum $\vec{p}_p$ in the LAB frame, the Υ momentum $\vec{p}_\Upsilon$ in the LAB frame and the μ^+ momentum $\vec{p}_\mu$ in the Υ rest frame.
The production plane is defined by the vectors $\vec{p}_p$ and $\vec{p}_\Upsilon$. For this analysis, the decay coordinate system $(\hat{x}, \hat{y}, \hat{z})$ is then defined by the following conditions:

- $\hat{z}$ lies along $\vec{p}_\Upsilon$;
- $\hat{y}$ is the normal to the production plane, lying along $\vec{p}_p \times \vec{p}_\Upsilon$;
- $\hat{x}$ completes the right-handed coordinate system $\hat{x} = \hat{y} \times \hat{z}$.

The Υ state vector can be chosen in the angular momentum eigenstate basis $|j, m\rangle$, whereas the final state $|\hat{p}, \lambda_+\lambda_-\rangle$. $\hat{p}$ can be expressed in terms of the two helicities of the decay products and of the direction $\hat{p}$ of the decay particles momenta in the Υ rest frame ($\vec{p}_{\mu^+}$ and $-\vec{p}_{\mu^-}$).
For the calculation of a decay-amplitude we have to express the initial and the final state in the same basis; the plane wave state $|\hat{p}, \lambda_+\lambda_-\rangle$ can be expanded in angular momentum eigenstates according to:

$$|\hat{p}, \lambda_+\lambda_-\rangle = \sum_{jm} |jm\lambda_+\lambda_-\rangle \sqrt{\frac{2j+1}{4\pi}}\, D^j_{m\lambda}(\phi, \theta, 0) \tag{A.2}$$

where $\lambda = \lambda_+ - \lambda_-$ and $D^j_{m\lambda}(\phi, \theta, 0)$ are Wigner functions:

$$D^j_{mm'}(\alpha, \beta, \gamma) = e^{-im\alpha} d^j_{mm'}(\beta) e^{-im'\gamma} \tag{A.3}$$

The $d^j_{mm'}(\beta)$ are real functions and satisfy

$$d^j_{m'm} = (-1)^{m-m'} d^j_{mm'} = d^j_{-m-m'}(\beta)$$

of the wave-function is composed by three vectors: $\langle 1\ 1| = (1\ 0\ 0)$, $\langle 1\ 0| = (0\ 1\ 0)$ and $\langle 1\ -1| = (0\ 0\ 1)$. We have therefore:

$$\langle 1\ 1|\rho|1\ 1\rangle = \rho_{11} \quad \langle 1\ 0|\rho|1\ 0\rangle = \rho_{00} \quad \langle 1\ -1|\rho|1\ -1\rangle = \rho_{-1-1}.$$

which allows all the necessary d functions for this calculation to be derived from:

$$d^1_{11}(\beta) = \frac{1+cos\beta}{2} \qquad d^1_{10}(\beta) = \frac{-sin\beta}{\sqrt{2}} \qquad d^1_{1-1}(\beta) = \frac{1-cos\beta}{2}. \tag{A.4}$$

The amplitude for the decay $\Upsilon \to \mu^+\mu^-$ from a given state $|j\ m\rangle$ to the state $|\widehat{p}\lambda_+\lambda_-\rangle$ is:

$$A_m(\widehat{p}\lambda_+\lambda_-) = \langle \widehat{p}\lambda_+\lambda_-|U|jm\rangle \tag{A.5}$$

where U is an operator that is invariant under rotations and reflections (we assume that parity is conserved), but whose detailed form and energy dependence does not concern us. By means of (A.2) the decay amplitude can be written:

$$A_m(\widehat{p}\lambda_+\lambda_-) = \sqrt{\frac{2j+1}{4\pi}}\ \langle jm\lambda_+\lambda_-|U|jm\rangle\ D^j_{m\lambda}{}^*(\phi,\theta,0) \tag{A.6}$$

Since U is a scalar under rotations, its matrix element depends on λ_+ and λ_-, but not on m. We therefore abbreviate it in an obvious way to $M(\lambda_+\lambda_-)$.
The square of the amplitude (A.5), summed over the helicities λ_+ and λ_- is proportional to the probability for the decay $\Upsilon \to \mu^+\mu^-$ into the direction $\widehat{p}$ from a state of definite z-component of angular momentum m.
Now we have to consider all the possible values of m and, if the decay of the resonant state Υ is described by a density matrix ρ, the angular distribution of the decay canbe written according to:

$$W(\theta,\phi) = N \sum_{mm'} \sum_{\lambda_+\lambda_-} A_m(\widehat{p}\lambda_+\lambda_-)\ \rho_{mm'}\ A^*_{m'}(\widehat{p}\lambda_+\lambda_-) \tag{A.7}$$

where N is a normalization constant. With the explicit form (A.6) this can be written as:

$$W(\theta,\phi) = N' \sum_{mm'} \sum_{\lambda_+\lambda_-} |M(\lambda_+\lambda_-)|^2\ D^j_{m\lambda}{}^*(\phi,\theta,0)\ D^j_{m'\lambda}(\phi,\theta,0)\ \rho_{mm'} \tag{A.8}$$

where $\lambda = \lambda_+ - \lambda_-$.

The angular distribution (A.8) can be put in various equivalent and manifestly real forms; for example, considering

$$Z^{j\lambda_\pm}_{mm'}(\theta) = d^j_{m\lambda}(\theta)d^j_{m'\lambda}(\theta) \pm d^j_{m-\lambda}(\theta)d^j_{m'-\lambda}(\theta)$$

we can find:

$$W(\theta,\phi) = N' \sum_{mm'} \sum_{\lambda_+\lambda_-} |M(\lambda_+\lambda_-)|^2\ Z^{j\lambda_\pm}_{mm'}(\theta)\ Re(\rho_{mm'}e^{i(m-m')\phi}) \tag{A.9}$$

and, summing over λ_+ and λ_-, simplifying the Wigner functions, we can write:

$$W(\theta,\phi) \propto \sum_{mm'} \rho_{mm'}\ e^{i(m-m')\phi}\ (d^1_{m1}(\theta)d^1_{m'1}(\theta) \pm d^1_{m-1}(\theta)d^1_{m'-1}(\theta)). \qquad \text{(A.10)}$$

This form allows us to determine the relation (2.2) by substituing the d function with (A.4) and considering that, since the $\widehat{z}$ axis lies in the production plane, parity conservation imposes further constraints on ρ:

$$\rho_{-1-1} = \rho_{11}$$

$$\rho_{-11} = \rho_{1-1}$$

$$\rho_{-10} = -\rho_{10}$$

$$\rho_{0-1} = -\rho_{01}$$

We therefore find:

$$W(\theta,\phi) \propto \frac{1+\rho_{00}}{2}\left(1+\frac{1-3\rho_{00}}{1+\rho_{00}}cos^2\theta\right) + \rho_{1-1}\ cos2\phi\ (1-cos^2\theta) \qquad \text{(A.11)}$$

$$+\sqrt{2}\ Re(\rho_{01})\ cos\phi\ sin2\theta \qquad \text{(A.12)}$$

With the change of variable $\alpha = \frac{1-3\rho_{00}}{1+\rho_{00}}$, the first term becomes the familiar expression $\propto (1+\alpha cos^2\theta)$. The other two terms depend on $cos2\phi$ and $cos\phi$, which both vanish when integrated over ϕ. In the polarization analysis, the data and Monte Carlo samples are always integrated over ϕ so these two terms can be ignored.

Appendix B

Quadratic fit: error on the parameters

When a Least Squares method is used to fit a sample with a 2-parameters quadratic shape (e.g. the $cos\theta$ spectrum, where θ is the polarization angle), the error on the parameter which multiplies the quadratic factor depends on the normalization parameter. In this Appendix an analytical explanation of such a dependence is carried out.

B.1 Quadratic Fit

The fit to a y set of data which is supposed to be quadratically distributed in the quantity x is done with the fitting function:

$$f(x) = p_0(1 + \alpha x^2)$$

where p_0 and α are the parameters to be tuned by the fitting procedure.

The function which has to be minimized in the Least Squares approach is:

$$\begin{aligned} S &= \sum_{i=1}^{n} \left[\frac{y_i - f(x_i)}{\sigma_i} \right]^2 \\ &= \sum_{i=1}^{n} \left[\frac{y_i - p_0(1 + \alpha x_i^2)}{\sigma_i} \right]^2 \end{aligned}$$

where i runs over the bins of the histogram which has to be fitted. The matrix

$$\mathcal{V} = \begin{pmatrix} \sigma {p_0}^2 & cor. \\ cor. & \sigma \alpha^2 \end{pmatrix}$$

is obtained by the S quantity by considering that:

$$\mathcal{V}^{-1} = \frac{1}{2} \begin{pmatrix} \dfrac{\partial^2 S}{\partial p_0^2} & \dfrac{\partial^2 S}{\partial p_0 \partial \alpha} \\ \\ \dfrac{\partial^2 S}{\partial \alpha \partial p_0} & \dfrac{\partial^2 S}{\partial \alpha^2} \end{pmatrix}$$

The calculation is straightforward algebra:

$$\frac{\partial^2 S}{\partial p_0^2} = \sum_i \frac{2(1+\alpha x_i^2)^2}{\sigma_i^2} \qquad , \qquad \frac{\partial^2 S}{\partial \alpha^2} = \sum_i \frac{2 p_0^2 x_i^2}{\sigma_i^2}$$

$$\frac{\partial^2 S}{\partial p_0 \partial \alpha} = \sum_i \frac{4\alpha p_0 x_i^4 + 2 y_i x_i^2}{\sigma_i^2} = \frac{\partial^2 S}{\partial \alpha \partial p_0}$$

$$\Downarrow$$

$$\mathcal{V}^{-1} = \begin{pmatrix} \sum_i \dfrac{(1+\alpha x_i^2)^2}{\sigma_i^2} & \sum_i \dfrac{2\alpha p_0 x_i^4 + 2 y_i x_i^2}{\sigma_i^2} \\ \\ \sum_i \dfrac{2\alpha p_0 x_i^4 + 2 y_i x_i^2}{\sigma_i^2} & \sum_i \dfrac{2 p_0^2 x_i^2}{\sigma_i^2} \end{pmatrix}$$

Now, applying the matrix-invertion mechanism

$$\mathcal{M}^{-1} = \begin{pmatrix} a & b \\ c & d \end{pmatrix} \longrightarrow \mathcal{M} = \begin{pmatrix} \frac{d}{detM^{-1}} & \frac{-b}{detM^{-1}} \\ \frac{-c}{detM^{-1}} & \frac{a}{detM^{-1}} \end{pmatrix}$$

we can find that:

$$det\mathcal{V}^{-1} = \sum_i \frac{(1+\alpha x_i^2)^2}{\sigma_i^2} \sum_j \frac{p_0^2 x_j^4}{\sigma_j^2} - \left(\sum_i \frac{2\alpha p_0 x_i^4 + y_i x_i^2}{\sigma_i^2} \right)^2$$

$$\sigma\alpha^2 = \frac{1}{detV^{-}1} \cdot \sum_i \frac{(1+\alpha x_i^2)^2}{\sigma_i^2}$$

From this result we can find that if we assume that the p_0 parameter is big with respect to the α parameter and to the x_i values (which is our case) the error on α is proportional to the inverse of p_0:

$$\sigma\alpha \propto \frac{1}{p_0}.$$

Now, considering that the normalization factor decreases gradually while α enhances, this is the reason of the fact that $\sigma\alpha$ increases while α enhances.

List of Figures

List of Tables

Bibliography

[1] D0 Collaboration: V. M. Abazov. Measurement of the polarization of the $\upsilon(1s)$ and $\upsilon(2s)$ states in $p\bar{p}$ collisions at $\sqrt{s}$ =1.96 tev, 2008.

[2] K. Anikeev et al. B physics at the tevatron: Run ii and beyond, 2002.

[3] Ermias T. ATOMSSA. Hard probes 2008, 8-15 June 2008.

[4] Geoffrey T. Bodwin, Eric Braaten, and G. Peter Lepage. Rigorous qcd analysis of inclusive annihilation and production of heavy quarkonium. *ERRATUM-IBID.D*, 55:5853, 1997.

[5] Eric Braaten, Bernd A. Kniehl, and Jungil Lee. Polarization of prompt j/ψ at the fermilab tevatron. *Phys. Rev. D*, 62(9):094005, Sep 2000.

[6] Eric Braaten and Jungil Lee. Polarization of upsilon(ns) at the fermilab tevatron. *Phys. Rev. D*, 63(7):071501, Mar 2001.

[7] W. E. Caswell and G. P. Lepage. Effective lagrangians for bound state problems in qed, qcd, and other field theories. *Phys.Lett. B*, 167:437, 1986.

[8] Peter Cho and Mark B. Wise. Spin symmetry predictions for heavy quarkonia alignment. *Physics Letters B*, 346:129, 1995.

[9] ALICE Collaboration. Alice: Physics performance report, volume i. *Journal of Physics G: Nuclear and Particle Physics*, 30(11):1517–1763, 2004.

[10] ALICE Collaboration. Alice: Physics performance report, volume ii. *Journal of Physics G: Nuclear and Particle Physics*, 32(10):1295–2040, 2006.

[11] Robert J. Cropp. *A Measurement of the Polarization of the J/ψ Mesons Produced in High-Energy $p\overline{p}$ Collisions.* PhD thesis, University of Toronto, 2000.

[12] Abe et al. j/ψ and $\psi(2s)$ production in $p\overline{p}$ collisions at $\sqrt{s} = 1.8$ tev. *Phys. Rev. Lett.*, 79(4):572–577, Jul 1997.

[13] Abe et al. Production of j/ψ mesons from χ_c meson decays in $p\overline{p}$ collisions at $\sqrt{s} = 1.8$ tev. *Phys. Rev. Lett.*, 79(4):578–583, Jul 1997.

[14] K. Anikeev et al. B physics at the tevatron: Run ii and beyond, 2002.

[15] M.C. Abreu et al. The production of j/ψ in 200 gev/nucleon oxygen-uranium interactions. *Phys. Lett. B*, 220:471, 1989.

[16] M.C. Abreu et al. Anomalous j/ψ suppression in pb-pb interactions at 158 gev/c per nucleon. *Phys. Lett. B*, 410:337–343, 1997.

[17] M.C. Abreu et al. j/ψ, ψ' and drell-yan production in s-u interactions at 200 gev per nucleon. *Phys. Lett. B*, 449:128, 1999.

[18] N. Brambilla et al. *Heavy Quarkonium Physics.* Addison-Wesley, 2005.

[19] Rachid Guernane et al. Measuring the b-meson production cross section in 5.5 tev pb-pb collisions using semileptonic decay muons. 2005.

[20] P. Faccioli. Qwg workshop, October 18th 2007.

[21] E Scomparin (for the NA60 Collaboration). j/ψ production in in-in and p-a collisions. *Journal of Physics G: Nuclear and Particle Physics*, 34(8):S463–S469, 2007.

[22] H. Fritzsch. *Phys.Lett. B*, 67:217, 1977.

[23] F. Halzen. *Phys.Lett. B*, 69:105, 1977.

[24] B. L. Ioffe and D. E. Kharzeev. Quarkonium polarization in heavy ion collisions as a possible signature of the quark–gluon plasma. *Physical Review C*, 68:061902, 2003.

[25] J.D. Jackson. Particle and polarization angular distributions for two and three body decays. In C. DeWitt M. Jacob, editor, *High Energy Physics (Les Houches 1965)*, page 325. Gordon and Breach Science, 1965.

[26] M J Leitch. Rhic results on j/ψ. *Journal of Physics G: Nuclear and Particle Physics*, 34(8):S453–S462, 2007.

[27] J.F. Owens M. Glück and E. Reya. *Phys.Lett. D*, 17:2324, 1978.

[28] Luciano Maiani. Towards a new state of matter. *Nuclear Physics A*, 774:14, 2006.

[29] T. Matsui and H. Satz. j/ψ suppression by quark-gluon plasma formation. *Phys. Lett. B*, 178:416–422, 1986.

[30] H. Satz. Quarkonium binding and dissociation: The spectral analysis of the qgp. *Nucl. Phys. A*, 783:249c–260c, 2007.

[31] E. Scomparin. J/ψ production in in-in and p-a collisions, 2007.

[32] P. Shukla. Glauber model for heavy ion collisions from low energies to high energies, 2001.

[33] B. A. Thacker and G. Peter Lepage. Heavy-quark bound states in lattice qcd. *Phys.Lett. D*, 43(1):196–208, 1991.

[34] W.Y. Keung V.D. Barger and R.J. Phillips. *Phys.Lett. B*, 91:253, 1980.